

**Reevaluating the Holographic Light-Front Meson Wave Function Using
Longitudinal Dynamics Obtained From the 't Hooft Equation**

BY

Spencer Keller

A thesis submitted to the
Department of Physics
Mount Allison University
in partial fulfillment of the requirements for the
Bachelor of Science degree
with Honours
May, 2022

ABSTRACT

The goal of this work is to investigate the effects of using a solution derived from the 't Hooft equation as the longitudinal mode for the light-front meson wave function in holographic Quantum Chromodynamics (hQCD). We calculate observables such as the mass spectra, decay constants, and charge radii for several mesons. We attempt to incorporate dynamical spin effects into our results, as this has led to better agreement with observation for the decay constant and charge radius in previous works. We also compare the parton distribution functions obtained through this approach to results obtained by Brodsky and de Téramond, who use a different approach. Some differences between the methods employed to calculate Transition Form Factors (TFFs) using these new dynamics and Light Cone Sum Rules (LCSR) are noted, but the results obtained in this investigation are preliminary. Finally, we find that this approach produces a mass spectrum that agrees well with observation for numerous pseudoscalar mesons, but predicts nonphysical answers for certain observables upon inclusion of spin structure.

ACKNOWLEDGMENTS

I would first like to thank my supervisors Dr. Ahmady and Dr. Sandapen (Acadia University) for their invaluable guidance and infinite patience with me throughout my time as a research assistant. Furthermore, I would like to thank my research partners, Idriss, Cameron, and Sugee for their valuable discussion and input on my project. I am also very grateful to Dr. Mondal, Neetika Sharma, and Dr. Kaur.

Finally, I would like to thank all of my friends who encouraged me to pursue an honours thesis, and supported me as I completed it. I would not have been able to do any of this without their unwavering support.

Contents

ABSTRACT	i
ACKNOWLEDGMENTS	ii
TABLE OF CONTENTS	iii
LIST OF FIGURES	iv
LIST OF TABLES	vii
GLOSSARY	ix
1 INTRODUCTION	1
1.1 Motivation	1
1.2 The Standard Model	2
1.2.1 Quantum Electrodynamics	4
1.2.2 Quantum Chromodynamics	5
1.3 Light-Front Holographic QCD	8
1.4 There's Just One Problem...	10
1.5 The Brodsky and de Téramond Prescription	11
1.6 Dynamical Spin Effects	12
2 Light-Front Formalism	14
2.1 Lorentz Transformations	14
2.2 Light-Front Coordinates	16
3 Using the 't Hooft Potential for the Longitudinal Mode of the Light-Front Wave Function	19
3.1 The 't Hooft Equation	19
3.2 Numerical Basis Functions	21
3.3 HQCD Using Longitudinal Dynamics Obtained From the 't Hooft Equation	23
3.4 Alternative Potential	26

4	Transition Form Factors for $B_s \rightarrow \phi$	29
4.1	QCDSR	29
4.2	LCSR	30
4.3	$B \rightarrow \pi$ Form Factors Using Overlap Formulas	38
5	Results	42
5.1	Meson Masses and Distribution Amplitudes	42
5.2	Decay Constants and Charge Radii	52
6	Discussion and Conclusion	56
	REFERENCES	58
A	Sample Code for Calculating Meson Masses	60

List of Figures

1.1	The Standard Model of elementary particle physics, which classifies each of the fundamental particles and force carriers and describes the interactions between subatomic particles via three of the four fundamental forces (strong nuclear force, weak nuclear force, and electromagnetism) [20].	3
1.2	The primitive electromagnetic vertex. An electron is depicted emitting or absorbing a photon. Note that this specific process is kinematically forbidden for real photons.	4
1.3	A Feynman diagram illustrating pair production between two photons, which produces an electron and positron pair.	5
1.4	The fundamental strong vertex. A quark is depicted emitting or absorbing a gluon.	6
1.5	An example of gluons coupling to themselves: A three gluon vertex. A similar diagram also exists for a four gluon vertex.	7
1.6	A system of two bound partons described in terms of LF coordinates. Here, $b_{\perp} = \vec{b} $ is the magnitude of the transverse separation between partons, P is the longitudinal momentum carried by the hadron, and x_1 and x_2 are the momentum fractions of the partons [21].	10
2.1	Illustrations of an instant form coordinate system (left) and a LF coordinate system (right) [10].	17
3.1	Comparison of bottomonium longitudinal modes coming from solutions to the 't Hooft equation using two different matrix sizes. The two solutions use 17 expansion coefficients (in red) and 7 expansion coefficients (in blue).	23
3.2	Pion longitudinal modes predicted by the 't Hooft equation using $\beta_1 = \beta_2 = 0.34$ (red) and the ansatz $X(x) = \mathcal{N}\sqrt{x\bar{x}} \exp\left[-\frac{m_q^2\bar{x}+m_q^2x}{2\kappa^2x\bar{x}}\right]$ (blue), where \mathcal{N} is a normalization constant.	26

4.1	The differential branching ratio for $B_s \rightarrow \phi\mu^+\mu^-$ as predicted by hQCD (red rectangles) and QCDSR (blue rectangles). The uncertainty widths are due to the form factors. The experimental data points are measured by LHCb [5].	37
5.1	Predictions for various ground state meson mass values using an increasing number of expansion coefficients, r , in the numerical solution to the 't Hooft equation (red) and in the expansion from Brodsky and de Téramond given by equation 3.16 (blue). The horizontal black lines are the observed masses.	44
5.2	Predictions for Regge slopes of the pion and its orbitally/radially excited states up to $n_T = 2$, using the 't Hooft equation to predict the square of the longitudinal mass.	44
5.3	Predictions for the light quark mass and coupling constant combination that will produce the greatest agreement (lowest fractional difference) with experimental pion mass values (left) and our predictions for the light quark mass and coupling constant combination which will produce values of $\beta \geq 0.5$ in the ansatz $X(x) = \mathcal{N}x^{\beta_1}(1-x)^{\beta_2}$, where \mathcal{N} is a normalization factor (right). We vary both light quark masses.	46
5.4	Predictions for the strange quark mass and coupling constant combination that will produce the greatest agreement with experimental kaon mass values . We hold the light quark mass fixed at $m_q = 0.046$ GeV while varying the strange quark mass.	47
5.5	Predictions for the heavy quark mass and coupling constant combination that will produce the greatest agreement with experimental B mass values (left) and experimental D mass values (right). We hold the light quark mass fixed at $m_q = 0.046$ GeV while varying the bottom and charm quark masses.	47
5.6	Predictions for the heavy quark masses and coupling constant combination that will produce the greatest agreement with experimental bottomonium (η_b) mass values (left) and charmonium (η_c) mass values (right). We vary both bottom quark masses and charm quark masses in each case.	48

5.7	Pion longitudinal mode (left) and pdf (right) from a numerical solution to the 't Hooft equation in red, and the solution from Brodsky's analytical method in blue. The following parameters were used: $m_q = m_{\bar{q}} = 0.046$ GeV, $g = 0.128$ GeV, $\beta_1 = \beta_2 = 0.34$, and a matrix size of $r = s = 7$	49
5.8	Kaon longitudinal mode (left) and pdf (right) from a numerical solution to the 't Hooft equation in red, and the solution from Brodsky's analytical method in blue. The following parameters were used: $m_q = 0.357$ GeV, $m_{\bar{q}} = 0.046$ GeV, $g = 0.680$ GeV, $\beta_1 = 0.7$, $\beta_2 = 0.35$, and a matrix size of $r = s = 9$	49
5.9	B longitudinal mode (left) and pdf (right) from a numerical solution to the 't Hooft equation in red, and the solution from Brodsky's analytical method in blue. The following parameters were used: $m_q = 4.64$ GeV, $m_{\bar{q}} = 0.046$ GeV, $g = 0.680$ GeV, $\beta_1 = 10$, $\beta_2 = 0.04$, and a matrix size of $r = s = 16$	50
5.10	Bottomonium longitudinal mode (left) and pdf (right) from a numerical solution to the 't Hooft equation in red, and the solution from Brodsky's analytical method in blue. The following parameters were used: $m_q = m_{\bar{q}} = 4.64$ GeV, $g = 0.523$ GeV, $\beta_1 = \beta_2 = 0.34$, and a matrix size of $r = s = 16$	50
5.11	Charmonium longitudinal mode (left) and pdf (right) from a numerical solution to the 't Hooft equation in red, and the solution from Brodsky's analytical method in blue. The following parameters were used: $m_q = m_{\bar{q}} = 1.37$ GeV, $g = 0.523$ GeV, $\beta_1 = \beta_2 = 0.34$, and a matrix size of $r = s = 16$	51

List of Tables

1.1	The four fundamental forces, their relative strengths, their effective ranges, the theory which describes them, and their corresponding force-carriers [17].	3
4.1	Predictions for the seven $B_s \rightarrow \phi$ form factors at $q^2 = 0$ using DAs obtained from QCDSR and hQCD. The uncertainty in the form factors comes from variation in strange quark mass (m_s) and the confinement scale (κ).	36
5.1	Quark masses and 't Hooft couplings in GeV. The confinement scale is fixed at $\kappa = 0.523$ GeV for all mesons.	42
5.2	Predictions for decay constants and charge radii of the ground state pion using the spin-improved wave function and the 't Hooft longitudinal mode and experimental values [16].	53
5.3	Predictions for decay constants and charge radii of the first excited state pion using the spin-improved wave function and the 't Hooft longitudinal mode.	54
5.4	Predictions for decay constants and charge radii of the second excited state pion using the spin-improved wave function and the 't Hooft longitudinal mode.	54
5.5	Predictions for decay constants and charge radii of the ground state kaon using the spin-improved wave function and the 't Hooft longitudinal mode and experimental values [16].	55
5.6	Predictions for decay constants and charge radii of the ground state B using the spin-improved wave function and the 't Hooft longitudinal mode and experimental values [16].	55

GLOSSARY

BdT	Brodsky and de Téramond
HLFQCD	Holographic Light-Front Quantum Chromodynamics
hQCD	Holographic Quantum Chromodynamics
LHCb	Large Hadron Collider beauty
LF	Light-Front
LFWF	Light-Front Wave Function
NLO	Next-to-Leading-Order
PDF	Parton Distribution Function
QCD	Quantum Chromodynamics
QCDSR	Quantum Chromodynamics Sum Rules
QED	Quantum Electrodynamics
SIWF	Spin-Improved Wave Function
TFF	Transition Form Factor

Chapter 1

INTRODUCTION

1.1 Motivation

The motivation of this thesis is to explore a different way to find the meson wave function and its transition form factors (TFFs). Traditionally, decay observables in the Standard Model (SM) are found using QCD Sum Rules (QCDSR); a non-perturbative framework used to find meson Distribution Amplitudes (DAs).

However, Ahmady et. al. have recently found that using input DAs obtained from hQCD in LCSR produce more accurate predictions of the differential branching ratio for various rare B decays [1]. This provides an impetus to explore other approaches using hQCD which incorporate longitudinal dynamics.

This is because in the conformal limit where hQCD is formulated, quarks are taken to be massless. In addition, hQCD predicts zero mass for low-lying pseudoscalar mesons like the pion and the kaon. While these results are what we would expect, they are nonetheless nonphysical as quarks have non-zero mass. This is our motivation for introducing the 't Hooft equation: A step beyond the semiclassical approximation to hQCD that takes into account quark mass contributions. This paper will explore how combining results from the 't Hooft equation and hQCD lead to excellent agreement with experimental data.

1.2 The Standard Model

The Standard Model of particle physics aims to describe each of the fundamental particles and their interactions with one another via three of the four fundamental forces: The strong nuclear force, the weak nuclear force, and electromagnetism. All (ordinary) matter is comprised of fundamental particles.

Elementary particles may be divided into four categories, as illustrated in Figure 1.1: Quarks (in purple), leptons (in green), gauge bosons (in red), and the Higgs boson (in yellow). Quarks and leptons - broadly referred to as fermions - are what constitute matter, and the resulting forces between them are generated by the exchange of bosons (also referred to as force-carrier particles or mediators).

Furthermore, quarks and leptons are organized into three generations in the SM: The first generation contains the lightest and most stable particles (the up quark, down quark, electron, and electron neutrino) whereas the third generation contains the heaviest and least stable particles (the top quark, bottom quark, tau, and tau neutrino). As such, heavier particles will tend to decay into lighter particles at a rate proportional to the mass difference between the initial particle and its products, unless prohibited by a conservation law [17].

Each of these particles possess a mass, electric charge, and spin that differentiate them from others in the model. Chief among these differentiating qualities is spin: Namely, fermions possess half-integer spin, whereas bosons possess integer spin.

The fundamental forces between fermions in the Standard Model are mediated by different bosons. The strong nuclear force is mediated by the exchange of gluons, and is responsible for the strong attractive force felt by quarks and in weaker form by nucleons (protons and neutrons) at very small distances. The weak nuclear force is mediated by the transfer of neutral Z bosons and charged W bosons, which are involved in particle decays at even smaller distances. Finally, the electromagnetic

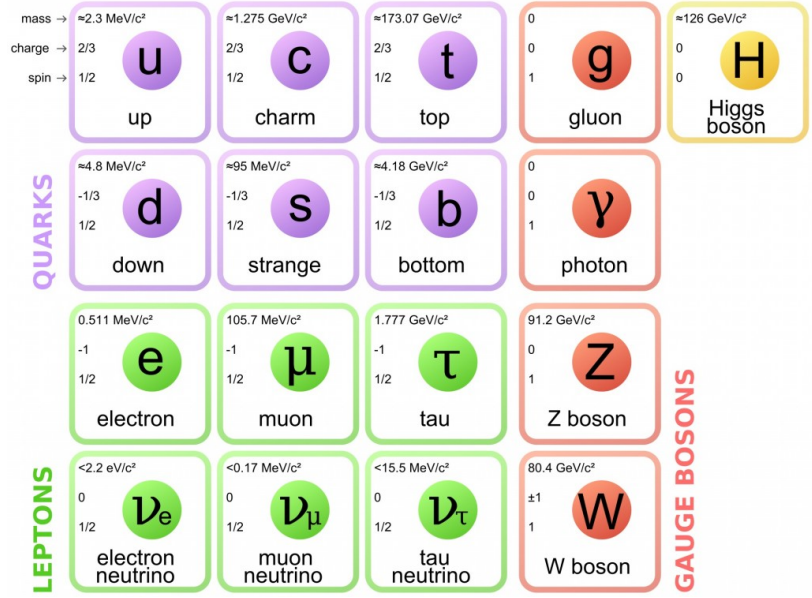


Figure 1.1: The Standard Model of elementary particle physics, which classifies each of the fundamental particles and force carriers and describes the interactions between subatomic particles via three of the four fundamental forces (strong nuclear force, weak nuclear force, and electromagnetism) [20].

force is mediated by the exchange of photons and acts over an infinite range. See Table 1.1 for quantitative information on the fundamental forces.

Force	Strength	Range	Theory	Mediator
Strong	10	10^{-15} m	Chromodynamics	Gluon
Electromagnetic	10^{-2}	Infinite	Electrodynamics	Photon
Weak	10^{-13}	10^{-18} m	Flavordynamics	W and Z
Gravitational	10^{-42}	Infinite	General Relativity	-

Table 1.1: The four fundamental forces, their relative strengths, their effective ranges, the theory which describes them, and their corresponding force-carriers [17].

The graviton is a hypothesized boson responsible for mediating the gravitational force. While the gravitational force is well-understood at macroscopic scales thanks to Einstein’s General Theory of Relativity, our understanding of gravity at microscopic scales is limited; a successful theory of quantum gravity has yet to be developed and a graviton has not been detected experimentally - hence its exclusion from the SM.

In addition to ordinary matter, there exists antimatter (also referred to as ordinary matter so as to differentiate it from dark matter), which possesses some qualities opposite to those of matter. For example, an "anti-electron" (known as a positron) has the same mass and spin as the electron, but opposite charge. That is, a positron has a mass of $0.511 \text{ MeV}/c^2$, spin $\frac{1}{2}$, and an electric charge of $1 e$.

1.2.1 Quantum Electrodynamics

Quantum electrodynamics (QED) is the oldest and most successful theory describing elementary particle interactions [17]. It describes the interactions between particles which carry electric charge based on the electromagnetic process shown in Figure 1.2:

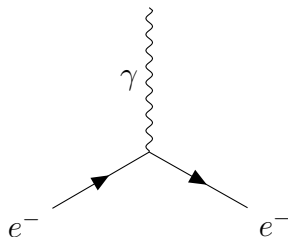


Figure 1.2: The primitive electromagnetic vertex. An electron is depicted emitting or absorbing a photon. Note that this specific process is kinematically forbidden for real photons.

Feynman diagrams like the one above are used to depict fundamental particle interactions across the SM. While these diagrams do not feature spatial dimensions, they *do* include a time axis which points horizontally to the right. This is why an electron can be understood to either absorb or emit a photon in this instance.

The mediator for the electromagnetic force is the photon. However, several electromagnetic processes may proceed via the transfer of other virtual particles. For example, pair production between two photons proceeds via the transfer of a virtual electron:

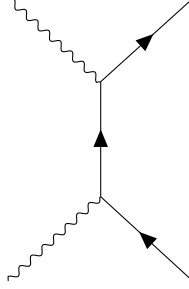


Figure 1.3: A Feynman diagram illustrating pair production between two photons, which produces an electron and positron pair.

Each electromagnetic vertex conserves various properties including momentum, energy, and electric charge. Feynman rules are used to better describe Feynman diagrams quantitatively [17]. This is partially achieved using the dimensionless fine structure constant, $\alpha_{em} = \frac{e^2}{\hbar c} = \frac{1}{137}$, which is proportional to the coupling strength between an electrically charged particle and an electric field with which it is interacting (i.e., a photon).

We can construct an infinite number of diagrams with an increasing number of vertices describing the same process. Each vertex contributes α_{em} to the sum, and vertices in the same diagram are compounded via multiplication. For example, since there are two vertices in Figure 1.3, it is proportional to α_{em}^2 .

However, since α_{em} is small, summing over powers of the fine structure constant for every diagram in this way will lead to progressively smaller contributions. This means these infinite sums can be truncated and are usually limited to no more than four terms [17]. This sum gives us an idea of the strength of coupling between electrons and photons in a particular process.

1.2.2 Quantum Chromodynamics

Quantum chromodynamics (QCD) describes interactions involving the strong nuclear force, which deals with interactions between particles carrying color charge. Not

unlike electric charge, color charge must be conserved. This helps to determine how various interactions proceed.

Feynman diagrams depicting strong interactions feature the fundamental strong vertex:

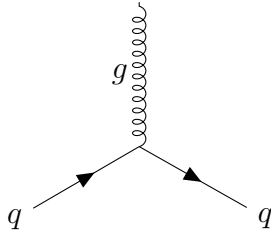


Figure 1.4: The fundamental strong vertex. A quark is depicted emitting or absorbing a gluon.

In contrast to electric charge, there are six kinds of colour charge, which we call red, blue, or green for quarks, and antired, antiblue, or antigreen for antiquarks.

It is necessary to introduce the notion of colour charge in order to satisfy the Pauli Exclusion Principle. That is, since two or more quarks, in this case, may not occupy the same quantum state in a quantum system (owing to the fact that quarks are spin $1/2$ particles), they must possess an additional differentiating quality: Colour charge. This convention also explains why quark bound states come in either pairs or triplets.

Gluons and quarks both possess colour charge, meaning that while gluons are certainly capable of interacting with quarks, they may also interact or couple with each other. This allows for more exotic bound states, such as a glueball - a bound state consisting only of gluons.

Yet another difference between QCD and QED is the determination of the strength of an interaction. Recall that in QED, we simply sum over the contribution of each vertex from a certain number of diagrams. Contrarily, the coupling constant in QCD, α_s , can be larger than one. Thus, instead of contributing increasingly smaller terms, successive diagrams contribute increasingly *more* in this regime, and so the answer

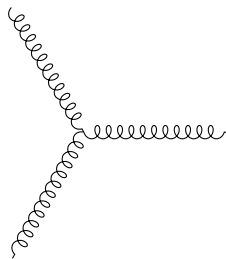


Figure 1.5: An example of gluons coupling to themselves: A three gluon vertex. A similar diagram also exists for a four gluon vertex.

obtained using the perturbative method (as in QED) will be divergent.

It was later discovered that this coupling constant is not in fact constant; but instead depends on the separation between two interacting particles; becoming small at short distances. As such, we call α_s a *running constant*.

The dependence of coupling strength on particle separation is known as *asymptotic freedom*. Asymptotic freedom implies that the coupling strength between quarks with very small separation (say, between quarks confined in a hadron) is minimal, meaning they interact relatively weakly via the strong force. Therefore, it is only possible to approximate a free quark at high energies, when the coupling strength between confined quarks is weak.

Variations in the size of the coupling constant described by asymptotic freedom may be understood through analogy to the screening effect caused by vacuum polarization in QED, wherein a vacuum behaves similarly to a dielectric material by spontaneously creating virtual electron-positron pairs. These pairs form an electric dipole which can partially screen a charged particle. Hence, the closer one gets to a charged particle, the less its charge will be screened. Similarly, vacuum polarization in QCD spontaneously generates virtual gluons and quarks which reduce coupling strength at short distances.

Asymptotic freedom leads to a phenomenon known as colour confinement: As the separation between quarks increases, so does the coupling strength between them. In

turn, the energy required to separate them increases. Eventually, it becomes more energetically favourable for new quark bound states (typically in the form of mesons) to be created rather than separate the existing quarks. This phenomenon prohibits the existence of any isolated particle possessing colour charge.

1.3 Light-Front Holographic QCD

In QCD, perturbation theory is the only avenue which allows us to obtain rigorous numerical results. However, several vital results in particle physics - such as hadron masses - may not be found using perturbation theory. As such, to gain insight about certain interactions and particle structures, we must resort to models that best agree with strong interaction characteristics. [21].

Specifically, we use a semiclassical approximation to QCD, wherein quantum loops are neglected [21]. In addition, it is convenient to use light-front (LF) coordinates in this regime, given that it deals with relatively light quarks and hence, the kinematics in the semiclassical approximation are highly relativistic. LF coordinates will be explored further in Chapter 2.

In order to derive the holographic LF wave function for mesons, we begin with the $SU_c(3)$ invariant (3+1)-dimensional QCD Lagrangian with the assumption that $N_c = 3$:

$$\mathcal{L}_{QCD} = \bar{\Psi}(i\gamma^\mu D_\mu - m)\Psi - \frac{1}{4}G_{\mu\nu}^a G^{a\mu\nu}, \quad (1.1)$$

which features two mass scales: the current quark mass, m , and the scale Λ_{QCD} in the running coupling [3]. The QCD Lagrangian is written using the familiar “instant form” coordinates (in contrast to light-front coordinates).

On the right-hand side of equation 1.1, Ψ is the valence light-front meson wave

function, $D_\mu = \partial_\mu - ig_s A_\mu^a T^a$, $G_{\mu\nu}^a = \partial_\mu A_\nu^a - \partial_\nu A_\mu^a + g_s c^{abc} A_\mu^b A_\nu^c$, and $[T^a, T^b] = ic^{abc} T^c$. Here, $G_{\mu\nu}^a$ is the gauge invariant gluon field strength tensor, A_μ^a are the gluon fields, and T^a are infinitesimal $SU_c(3)$ generators.

To proceed further, we exploit the conformal limit in the Hamiltonian formulation of (3+1)-dim QCD on the light front, with $N_c = 3$ [3]. That is, by switching from instant form coordinates (which are used to define the QCD Lagrangian) to light-front coordinates and taking the limit in which quark masses and quantum loops are neglected, the valence meson light-front wave function factorizes as,

$$\Psi(x, \zeta, \varphi) = \frac{\Phi(\zeta)}{\sqrt{2\pi\zeta}} e^{iL\varphi} X(x), \quad (1.2)$$

where $x = k^+/P^+$ is the light-front momentum fraction carried by the quark. The transverse wave function, Φ , satisfies the holographic Schrödinger Equation [3]:

$$\left(-\frac{d^2}{d\zeta^2} - \frac{1 - 4L^2}{4\zeta^2} + U_T(\zeta) \right) \Phi(\zeta) = M_T^2 \Phi(\zeta) \quad (1.3)$$

with the oscillator potential given by [14]

$$U_T(\zeta, J) = \kappa^4 \zeta^2 + 2\kappa(J - 1), \quad (1.4)$$

where $\zeta = \sqrt{x\bar{x}}b_\perp$ is the transverse distance between the bound quarks, b_\perp is the magnitude of the transverse separation between the bound quarks, $\bar{x} = 1 - x$ is the momentum fraction carried by the antiquark, L is the maximum orbital angular projection of the meson, J is the meson's spin, and M is the mass of the meson.

The longitudinal mode may be fixed as $X(x) = \sqrt{x(1-x)}$ by the holographic mapping of the electromagnetic (or gravitational) form factor in physical spacetime [3]. Furthermore, now that both the longitudinal mode is known from the above

ansatz, and the transverse mode is known to come from the solution to the holographic Schrödinger equation, we find the complete, normalized wave function to be:

$$\Psi(x, \zeta) = \frac{\kappa}{\pi} \sqrt{x\bar{x}} \exp \left[-\frac{\kappa^2 \zeta^2}{2} \right]. \quad (1.5)$$

An illustration of the system described by these equations in LF coordinates may be found below. Note that in contrast to the above notation, this figure uses indices on its momentum fractions to discriminate between the momentum fraction of the quark and antiquark.

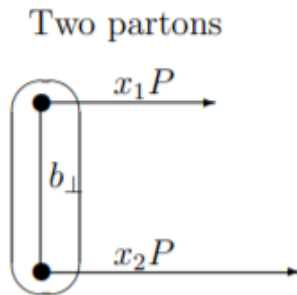


Figure 1.6: A system of two bound partons described in terms of LF coordinates. Here, $b_{\perp} = |\vec{b}|$ is the magnitude of the transverse separation between partons, P is the longitudinal momentum carried by the hadron, and x_1 and x_2 are the momentum fractions of the partons [21].

1.4 There's Just One Problem...

A major success of hQCD is its ability to predict vanishing pion masses in the chiral (zero-mass quark) limit, as one would expect. To see this, look no further than the mass spectrum admitted by the holographic Schrödinger equation [3]:

$$M_T^2(n_T, J, L) = 4\kappa^2 \left(n_T + \frac{J+L}{2} \right). \quad (1.6)$$

where n_T is the radial quantum number. Specifically, notice that for the ground state pion ($n_T = J = L = 0$), the predicted meson mass is zero!

This spectrum also features a Regge-like linear dependence of the meson mass squared on the radial and orbital quantum numbers. As well, the confinement scale κ generates meson masses in the absence of quark masses and the scale Λ_{QCD} in the running coupling [3].

However, the “problem”[†] with hQCD is exactly the latter: Light-front holography does not admit non-zero quark masses! As such, it does not predict the physical pion mass. It is thus necessary to extend this approach to accommodate non-zero quark masses and reconcile its discrepancy with experiment.

1.5 The Brodsky and de Téramond Prescription

To account for nonzero quark masses (and hence non-zero light meson masses), we follow Brodsky and de Téramond’s (BdT) prescription for the normalized holographic LF wave function for ground state mesons which goes beyond the semiclassical approximation [11]:

$$\Psi(x, \zeta^2) = \mathcal{N} \sqrt{x(1-x)} \exp\left[-\frac{\kappa^2 \zeta^2}{2}\right] \exp\left[-\frac{m_q^2 \bar{x} + m_{\bar{q}}^2 x}{2\kappa^2 x \bar{x}}\right] \quad (1.7)$$

where the longitudinal mode now has the appended exponential term, $\exp\left[-\frac{m_q^2 \bar{x} + m_{\bar{q}}^2 x}{2\kappa^2 x \bar{x}}\right]$.

Notice that in the chiral limit, this reduces back to $X(x) = \sqrt{x\bar{x}}$.

The above wave function uses the invariant mass ansatz, which includes the expression for the light-front kinetic energy with quark masses. For a two-parton state,

[†]Quotes are used around, “problem” because this feature of hQCD stems from the way it is formulated: In the conformal limit! While this is an expected outcome, it is still desirable to account for non-zero quark masses and predict physical meson masses across the whole range of quantum numbers.

this amounts to substituting [15]

$$\frac{\mathbf{b}_\perp^2}{x\bar{x}} \rightarrow \frac{\mathbf{b}_\perp^2}{x\bar{x}} + \frac{m_q^2}{x} + \frac{m_{\bar{q}}^2}{\bar{x}} \quad (1.8)$$

in the ground-state Gaussian wave function. Conveniently, the substitution is also the invariant mass squared of the $q\bar{q}$ pair: $s = (p_q + p_{\bar{q}})^2$ [15].

The longitudinal and transverse modes are normalized as

$$\int_0^1 X^2(x) dx = 1 \quad (1.9)$$

and

$$\int_0^1 \Phi^2(\zeta) d\zeta = 1. \quad (1.10)$$

1.6 Dynamical Spin Effects

So far we have not considered the spin of quarks. Following the method employed in [6], we find that the spin-improved wave function is given by:

$$\Psi_{h,\bar{h}}^P(x, \mathbf{b}) = [AMx\bar{x} + B(xm_f + \bar{x}m_{\bar{f}})]h\delta_{h,-\bar{h}} + iBh\partial_b\delta_{h,\bar{h}} \frac{\Psi(x, \zeta^2)}{x\bar{x}} \quad (1.11)$$

where h and \bar{h} are the helicities of the quark and antiquark, respectively. The wave function $\Psi(x, \zeta^2)$ now follows the BdT prescription given in equation 1.7. It is normalized such that

$$\int d^2\mathbf{b}dx |\Psi^p(x, \mathbf{b}^2)|^2 = 1 \quad (1.12)$$

with

$$|\Psi^P(x, \mathbf{b}^2)|^2 = \sum_{h, \bar{h}} |\Psi_{h, \bar{h}}^P(x, \mathbf{b}^2)|^2. \quad (1.13)$$

In equation 1.11, A and B are dimensionless, arbitrary constants, where B is referred to as the dynamical spin parameter [6]. This is because as $B \rightarrow 0$, the spin-improved wave function reduces to the original holographic wave function (meaning the spins of the quarks decouple from their dynamics), and as $B \rightarrow \infty$, the spin effects are maximal.

For the purposes of calculating observables in chapter 5, we can take $A = 1$. However, it is interesting to note that taking $A = \frac{\kappa}{\sqrt{2\pi M}}$ and $B = 0$ causes the spin-improved wave function to reduce exactly to the *normalized* holographic wave function (equation 1.7).

Chapter 2

Light-Front Formalism

We are now going to digress for a moment to talk about light-front formalism - an aspect so vital to *light-front* holography that it makes up 2/3 of the name!

2.1 Lorentz Transformations

According to classical physics, we may use the following set of linear transformations, known as Galilean transformations, to switch from one inertial reference frame (taken to be at rest) to another reference frame travelling at a constant speed v in the z direction:

$$t' = t$$

$$x' = x$$

$$y' = y$$

$$z' = z - vt,$$

where t is the time elapsed since some arbitrary initial point in time, $t = 0$. The coordinates (t', x', y', z') give the temporal and spatial coordinates in the moving reference frame, whereas (t, x, y, z) give the coordinates in the rest frame.

However, Einstein's theory of special relativity showed that Galilean transformations are only valid approximations at low velocities, $v \ll c$, where $c = 2.99 \times 10^8$ m/s is the speed of light. As we approach relativistic speeds (velocities that are a significant fraction to the speed of light), this approximation breaks down due to

time dilation and spatial contraction. Since the laws of physics must remain the same in every inertial reference frame, we use Lorentz transformations to switch between them:

$$ct' = \gamma \left(ct - \frac{vz}{c} \right) \quad (2.1)$$

$$x' = x \quad (2.2)$$

$$y' = y \quad (2.3)$$

$$z' = \gamma \left(z - \frac{v}{c} ct \right), \quad (2.4)$$

where $\gamma = \frac{1}{\sqrt{1-\frac{v^2}{c^2}}}$ is the Lorentz factor, and the term $\frac{v}{c}$ is typically represented as β . We express the time coordinate as ct so that each coordinate is in units of meters. Additionally, we may express any Lorentz transformation as a linear transformation using the Lorentz matrix:

$$\Lambda = \begin{bmatrix} \gamma & 0 & 0 & -\gamma\beta \\ 0 & 1 & 0 & 0 \\ 0 & 0 & 1 & 0 \\ -\gamma\beta & 0 & 0 & \gamma \end{bmatrix} \quad (2.5)$$

Note that this matrix specifically describes a Lorentz transformation for inertial frames moving in the z -direction. In order to adjust it for Lorentz transformations along different spatial axes, we simply swap the fourth row with either the second or third rows, for a transformation in the x or y directions, respectively.

Therefore, taking the product of Λ with a position-time 4-vector, (ct, x, y, z) , yields

the corresponding 4-vector in prime coordinates:

$$\mathbf{x}' = \begin{bmatrix} ct' \\ x' \\ y' \\ z' \end{bmatrix} = \begin{bmatrix} \gamma & 0 & 0 & -\gamma\beta \\ 0 & 1 & 0 & 0 \\ 0 & 0 & 1 & 0 \\ -\gamma\beta & 0 & 0 & \gamma \end{bmatrix} \begin{bmatrix} ct \\ x \\ y \\ z \end{bmatrix}$$

Alternatively, this product may be expressed using Einstein summation notation:

$$x^{\mu'} = \Lambda_{\nu}^{\mu'} x^{\nu}, \quad (2.6)$$

where μ is the matrix's row index ($\mu = 0, 1, 2, 3$), and ν is its column index ($\nu = 0, 1, 2, 3$).

2.2 Light-Front Coordinates

In practice, Lorentz transformations applied in Cartesian coordinates can introduce an undesirable level of algebraic. Therefore, we introduce a new set of coordinates which reduce to scalar transformations under Lorentz boosts, known as light-front (LF) coordinates:

$$x^+ = ct + z \quad (2.7)$$

and

$$x^- = ct - z, \quad (2.8)$$

where x^+ gives the new time coordinate, x^- gives the new spatial coordinate, t is the usual time coordinate, and z is one of the usual Cartesian coordinates. We refer to the other coordinates (x and y under this convention) as \mathbf{x}_\perp . As in Cartesian coordinates, \mathbf{x}_\perp remains unaffected by Lorentz transformations.

Under this convention, the “instant-form” four-vector, $(x^0, x^1, x^2, x^3) = (ct, x, y, z)$ becomes $x = (x^+, x^-, \mathbf{x}_\perp)$. This naturally extends to momentum as well, with the momentum four-vector expressed as $P = (P^+, P^-, \mathbf{P}_\perp)$ with $P^\pm = P^0 \pm P^3$.

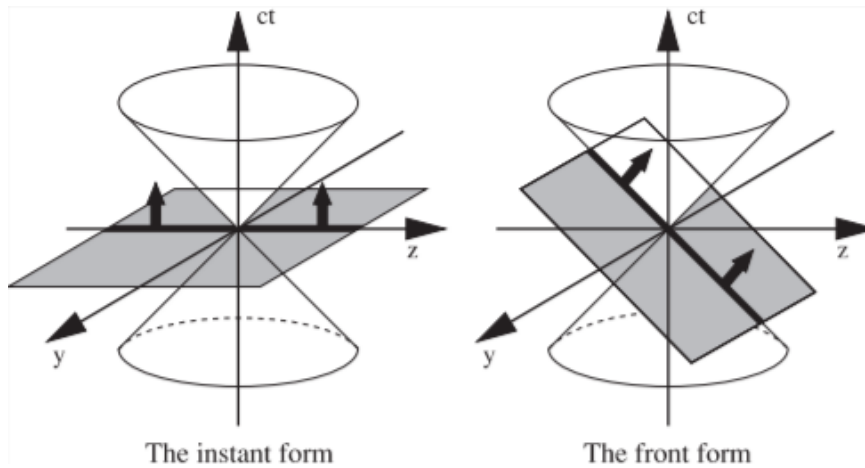


Figure 2.1: Illustrations of an instant form coordinate system (left) and a LF coordinate system (right) [10].

To demonstrate the Lorentz-invariance of LF coordinates, consider the effect of a Lorentz transformation in the z -direction on the above coordinates, noting that the x and y -coordinates remain unchanged. First, the transformed LF time coordinate is

given by:

$$\begin{aligned}
(x^+)' &= ct' + z' \\
&= (\Lambda_0^0 x^0 + \Lambda_1^0 x^1 + \Lambda_2^0 x^2 + \Lambda_3^0 x^3) + (\Lambda_0^3 x^0 + \Lambda_1^3 x^1 + \Lambda_2^3 x^2 + \Lambda_3^3 x^3) \\
&= (\gamma ct + 0 + 0 - \gamma\beta z) + (-\gamma\beta ct + 0 + 0 + \gamma z) \\
&= \gamma(ct[1 - \beta] + z[1 - \beta]) \\
&= \gamma(1 - \beta)(ct + z) \\
&= \frac{1 - \beta}{\sqrt{1 - \beta^2}} x^+ \\
&= \sqrt{\frac{1 - \beta}{1 + \beta}} x^+,
\end{aligned}$$

and the transformed LF spatial coordinate is given by:

$$\begin{aligned}
(x^-)' &= ct' - z' \\
&= (\Lambda_0^0 x^0 + \Lambda_1^0 x^1 + \Lambda_2^0 x^2 + \Lambda_3^0 x^3) - (\Lambda_0^3 x^0 + \Lambda_1^3 x^1 + \Lambda_2^3 x^2 + \Lambda_3^3 x^3) \\
&= (\gamma ct + 0 + 0 - \gamma\beta z) - (-\gamma\beta ct + 0 + 0 + \gamma z) \\
&= \gamma(ct[1 + \beta] - z[1 + \beta]) \\
&= \gamma(1 + \beta)(ct - z) \\
&= \frac{1 + \beta}{\sqrt{1 - \beta^2}} x^- \\
&= \sqrt{\frac{1 + \beta}{1 - \beta}} x^-.
\end{aligned}$$

Therefore, Lorentz transformations act on LF coordinates as scalar multiplication, where x^+ is multiplied by a factor of $\sqrt{\frac{1-\beta}{1+\beta}}$, and x^- is multiplied by a factor of $\sqrt{\frac{1+\beta}{1-\beta}}$ under Lorentz boosts in the z -direction.

Chapter 3

Using the 't Hooft Potential for the Longitudinal Mode of the Light-Front Wave Function

In section 1.5, we showed that we can account for non-zero quark masses in hQCD through the BdT prescription [11]. This prescription, along with an ostensibly universal $\kappa \approx 0.5$ GeV, have led to successful phenomenology of light mesons [3].

However, applying the BdT prescription to heavy mesons leads to $\kappa \propto \sqrt{m_Q}$, where m_Q is the heavy quark mass - which is both inconsistent with the Gell-Mann-Oakes-Renner (GMOR) relation for light quarks and provides evidence contradicting the existence of a universal κ . Attempts have been made to prevent this by using a different scale $\lambda \neq \kappa$, suggesting that the longitudinal mode is the solution to a different Schrödinger-like equation than that in equation 1.3 [3].

Venturing beyond both the semiclassical approximation and the BdT prescription, we search for an alternative solution to the holographic Schrödinger Equation that might successfully predict the full spectrum of mesons.

Introducing: The 't Hooft Equation.

3.1 The 't Hooft Equation

In the 70's, 't Hooft derived a Schrödinger-like equation for the longitudinal mode. They began from the (1+1)-dimensional QCD approximation and assumed $N_c \gg 1$, and came to the 't Hooft equation [19]:

$$\left(\frac{m_q^2}{x} + \frac{m_{\bar{q}}^2}{1-x} \right) \chi(x) + U_L(x)\chi(x) = M_L^2\chi(x) \quad (3.1)$$

where $X(x) = \sqrt{x(1-x)} \chi(x)$ is the longitudinal mode (the same one used in equation 1.2), and the longitudinal potential U_L is given by

$$U_L(x)\chi(x) = \frac{g^2}{\pi} \mathcal{P} \int dy \frac{\chi(x) - \chi(y)}{(x-y)^2}. \quad (3.2)$$

where \mathcal{P} denotes the principal value prescription and $g = g_s \sqrt{N_c}$ gives the 't Hooft coupling, which plays the same role as α_s in the QCD Lagrangian (equation 1.1) [3]. The ground state pseudoscalar meson masses are generated by g and the quark masses as $M_T = 0$ for these hadrons.

There exists a near exact analytic solution of the longitudinal mode for the ground state, which gives rise to the ansatz $\chi(x) = x^{\beta_1}(1-x)^{\beta_2}$ [14]. This approximation leads us to the transcendental equation:

$$\frac{m_i^2 \pi}{g^2} - 1 + \pi \beta_i \cot(\pi \beta_i) = 0 \quad (3.3)$$

Notice that the form $X(x) = \sqrt{x(1-x)}$ is recovered from equation 3.3 only if we take $\beta_1 = \beta_2 = 0$ in the conformal limit (as quark masses and the 't Hooft coupling go to zero).

Not only have we accounted for non-vanishing quark masses in hQCD by finding an alternative longitudinal mode to the BdT prescription, but we have also found a way to predict physical light meson masses. This is because we can find the longitudinal mass contribution as an eigenvalue of the 't Hooft equation, giving rise to the following mass spectrum:

$$M^2(n_L, n_T, J, L) = M_T^2(n_T, J, L) + M_L^2(n_L), \quad (3.4)$$

where M_T^2 is the familiar transverse contribution (equation 1.6) and n_L is the radial

quantum number. We will now explore exactly *how* we can find the longitudinal mode.

3.2 Numerical Basis Functions

To solve the 't Hooft equation, we use Chabysheva and Hiller's method [14], which begins with expanding the longitudinal mode $\chi(x)$ in terms of orthonormal basis functions f_r , given by

$$f_r(x) = N_r x^{\beta_1} (1-x)^{\beta_2} P_r^{(2\beta_2, 2\beta_1)}(2x-1), \quad (3.5)$$

where $P_r^{(2\beta_2, 2\beta_1)}$ is a Jacobi polynomial of order r , with normalization factor N_r :

$$N_r = \sqrt{(2r + \tilde{\beta}_1 + \tilde{\beta}_2) \frac{r! \Gamma(r + \tilde{\beta}_1 + \tilde{\beta}_2)}{\Gamma(r + \tilde{\beta}_1 + 1) \Gamma(r + \tilde{\beta}_2)}}. \quad (3.6)$$

In order to expand the longitudinal mode as

$$\chi(x) = \sum_r c_r f_r(x), \quad (3.7)$$

a set of expansion coefficients \vec{c} must first be obtained. This is done by diagonalizing the longitudinal equation in the chosen basis. Each expansion coefficient is obtained from the corresponding index in the eigenvector of the matrix representation given by

$$(m_1^2 A_1 + m_2^2 A_2 + g^2 B) \vec{c} = M_L^2 \vec{c}, \quad (3.8)$$

with matrices A_1 , A_2 , and B , where the eigenvalue M_L^2 gives the longitudinal meson mass squared. In other words, c_r is the r^{th} entry in the eigenvector $\vec{c} =$

$(c_0, c_1, c_2, \dots, c_r, \dots, c_k)$ in equation 3.8.

The aforementioned matrices are defined by

$$(A_1)_{rs} = \int_0^1 \frac{dx}{x} f_r(x) f_s(x), \quad (3.9)$$

$$(A_2)_{rs} = \int_0^1 \frac{dx}{1-x} f_r(x) f_s(x), \text{ and} \quad (3.10)$$

$$B_{rs} = \int_0^1 dx \mathcal{P} \int_0^1 dy f_r(x) \frac{f_s(x) - f_s(y)}{(x-y)^2}. \quad (3.11)$$

However, the potential term may be rewritten to make equation 3.11 symmetric, as such:

$$B_{rs} = \frac{1}{2} \int_0^1 dx \int_0^1 dy \frac{f_r(x) - f_r(y)}{x-y} \frac{f_s(x) - f_s(y)}{x-y}. \quad (3.12)$$

This not only resolves the principal value prescription introduced in 3.2, but introduces an explicit symmetry which simplifies the matrix diagonalization [14].

In addition, the size of the matrices used in the diagonalization determine the size of the eigenvector \vec{c} , and thus the number of expansion coefficients in 3.7. This is important in determining the correct expansion for a given meson, as successive terms in the eigenvectors do not converge to zero as quickly as meson mass increases, necessitating a larger number of expansion coefficients.

For example, the set of expansion coefficients for the ground state pion using matrix dimensions $r = s = 7$ yields

$$\vec{c} = (0.999, 0, -0.0397, 0, -0.00128, 0, -0.000260),$$

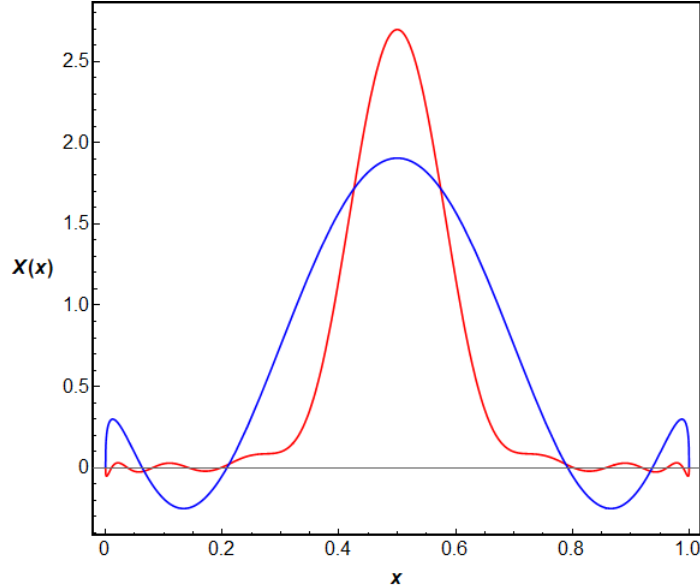


Figure 3.1: Comparison of bottomonium longitudinal modes coming from solutions to the 't Hooft equation using two different matrix sizes. The two solutions use 17 expansion coefficients (in red) and 7 expansion coefficients (in blue).

which converges to zero sufficiently quickly to justify a small matrix size. In contrast, using matrix dimensions $r = s = 7$ for the relatively heavy η_b meson yields

$$\vec{c} = (0.723, 0, -0.573, 0, 0.365, 0, -0.126).$$

Given the large number of contributing terms and slow convergence rate in this set of expansion coefficients, using a small matrix size in the expansion of $X(x)$ for η_b will not produce the desired level of accuracy in its longitudinal dynamics.

3.3 HQCD Using Longitudinal Dynamics Obtained From the 't Hooft Equation

Recall that in the hQCD regime, the ϕ wave function requires the additional exponential term to account for nonzero quark masses. Moreover, better agreement with

data for light mesons requires the inclusion of a dynamical spin structure [6]. We can alternatively account for non-zero quark masses using the 't Hooft equation and hQCD. In fact, we will see in chapter 5 that it is sometimes favourable *not* to include spin structure when this alternative longitudinal dynamics is used.

This distinction is perhaps most noticeable when making predictions for very light systems: Recall from the mass spectrum given by equation 4.4 that hQCD (without using the BdT prescription) predicts the transverse mass contribution for the pion to be zero. As a result, hQCD predicts massless pions.

In contrast, the 't Hooft equation predicts a longitudinal contribution of $M_L^2 = 0.0197 \text{ GeV}^2$. Along with the transverse contribution $M_T^2 = 0$ predicted by hQCD, the squared pion mass is $M_\pi^2 = M_L^2 + M_T^2 = 0.0197 \text{ GeV}^2$ or $M_\pi = 0.140 \text{ GeV}$, which is well within 1% of the observed value [16].

In addition, using the 't Hooft equation to find the longitudinal mode sets it apart from the “typical” hQCD approach. hQCD fixes $X(x)$ through a holographic mapping of the EM form factor in AdS_5 onto the 4-dimensional physical spacetime [3], giving us $X(x) = \sqrt{x\bar{x}}$.

In contrast to this ansatz, we can find longitudinal dynamics using the 't Hooft potential, which are obtained from solutions to equation 3.1. The method for finding these solutions is detailed in the previous section.

We have shown that the 't Hooft equation reproduces the familiar light-front holographic wave function provided the transcendental equation 3.3 is satisfied in the conformal limit (where the valence light-front meson wave function is formulated). In other words, equation 3.3 predicts $\beta_1 = \beta_2 = 0$ in the chiral limit.

However, this equation does not need to be satisfied beyond the conformal limit. For example, for up and down quark masses m_u and m_d , the 't Hooft Equation predicts that $M_\pi^2 \propto m_{u/d}$ in the chiral limit (the limit in which g is fixed and quark

masses go to zero). This is consistent with the Gell-Mann-Oakes-Renner (GMOR) relation [3].

In order to numerically solve the 't Hooft Equation, the solution $\chi(x)$ is expanded in terms of orthonormal basis functions according to equation 3.5. For $r = 0$, the Jacobi polynomial in this function is constant, meaning that it assumes the form $f_0(x) \propto x^{\beta_1}(1-x)^{\beta_2}$. In addition, the $r = 0$ term dominates successive terms in the expansion (as was demonstrated in the previous chapter), so it accounts for a large fraction of the probability in $\chi(x)$.

While the basis function strongly resembles the longitudinal mode obtained from light-front holography for $\beta_1 = \beta_2 = 1/2$, the longitudinal mode should be independent of the choice of β_1 and β_2 . Indeed, χ^2 minimization has revealed that an accurate solution is obtained in the fewest number of terms using $\beta_1 = \beta_2 = 0.34$ for the pion. This means that a choice of $\beta_1 = \beta_2 \neq 1/2$ still results in good agreement between the longitudinal dynamics of both approaches.

A comparison of the longitudinal modes obtained from hQCD (Brodsky and de Téramond's prescription) using the familiar potential (equation 1.4) and the 't Hooft potential is included in Figure 3.2.

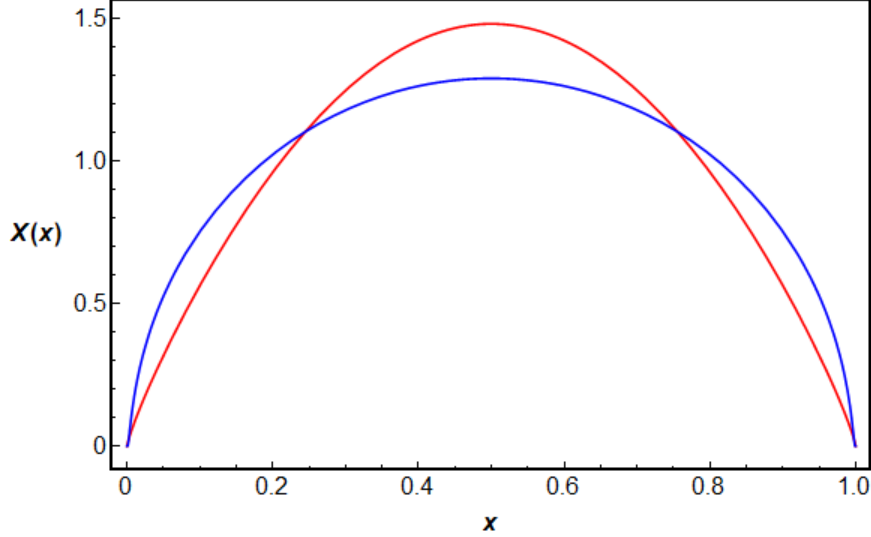


Figure 3.2: Pion longitudinal modes predicted by the 't Hooft equation using $\beta_1 = \beta_2 = 0.34$ (red) and the ansatz $X(x) = \mathcal{N} \sqrt{x\bar{x}} \exp \left[-\frac{m_q^2 \bar{x} + m_{\bar{q}}^2 x}{2\kappa^2 x\bar{x}} \right]$ (blue), where \mathcal{N} is a normalization constant.

3.4 Alternative Potential

Brodsky and de Téramond have put forward an alternative potential to the 't Hooft equation that uses a similar set of basis functions to compute the longitudinal mass contribution.

First, a different effective longitudinal potential is adopted:

$$U_L(x) = -\sigma^2 \partial_x (x(1-x)\partial_x), \quad (3.13)$$

where σ is fixed by the proportionality requirement between the mass scale and heavy meson masses: $\kappa = \sqrt{\sigma m_Q}$ (namely, $m_Q \geq 1.8$ GeV) [15].

The solution to the longitudinal LF Schrödinger Equation for this potential is given by [15],

$$\chi_n^{\alpha,\beta}(x) = N_n x^{\alpha/2} (1-x)^{\beta/2} P_n^{(\alpha,\beta)}(1-2x), \quad (3.14)$$

where $\alpha = \frac{2m_q}{\sigma}$ and $\beta = \frac{2m_{\bar{q}}}{\sigma}$ [15].

However, this solution lacks the exponential term which accounts for the LF kinetic energy with quark masses from equation 1.7. As Brodsky and de Téramond deem this to be a desirable characteristic for the longitudinal mode, we perform the following expansion to emulate the exponential behaviour for $\chi(x)$ [15]:

$$\mathcal{N} \exp \left[-\frac{\sigma}{8\kappa} \left(\frac{\alpha^2}{x} + \frac{\beta^2}{1-x} \right) \right] = \sum_r C_r \chi_r(x), \quad (3.15)$$

where \mathcal{N} is the normalization factor for the longitudinal mode. Using the orthonormality of $\chi_n(x)$, we can solve for each C_n by multiplying both sides by χ and integrating from $x = 0$ to $x = 1$.

This formulation also allows us to find the longitudinal mass contribution from the expansion coefficients, as such [15]:

$$M_L^2 = \sigma^2 \sum_r C_r^2 \nu^2(r, \alpha, \beta), \quad (3.16)$$

with eigenvalues $\nu^2(r, \alpha, \beta) = \frac{1}{4}(\alpha + \beta + 2r)(2 + \alpha + \beta + 2r)$.

It is important to note that, unlike when using the 't Hooft potential to find the longitudinal mode or mass spectrum, including contributions above $r = 20$ tends to introduce large amounts of uncertainty for light quarks [10].

The mass spectrum obtained using this potential also predicts a physical pion mass and accounts for non-zero quark masses. In fact, we will see in coming sections that this spectrum and the spectrum obtained using the 't Hooft potential are quite similar. This warrants questioning: If the longitudinal dynamics of both approaches are similar, will observables calculated using either approach also resemble one another? This query is addressed at length in Chapter 5.

While only observables obtained using the solution to the 't Hooft equation to

find the longitudinal mode will be considered in this paper, such a comparison would nonetheless be interesting.

Chapter 4

Transition Form Factors for $B_s \rightarrow \phi$

A reliable point of comparison for the accuracy of various methods used to compute meson wave functions is the transition form factor (TFF): A mathematical function parametrizing the hadronic matrix elements of decay observables.

TFFs are useful to this end since they are sensitive to their input distribution amplitudes (DAs), and colliders like the LHC and SuperKEK (so-called “B factories”) provide an abundance of experimental data which can be used for comparison to predictions.

In particular, the rare decay $B_s \rightarrow \phi\mu^+\mu^-$ provides a method to compare results obtained from using hQCD against other frameworks, which will be explored in this chapter.

4.1 QCDSR

QCDSR is the “traditional” method used to find transition form factors. Recall from Section 1.2.2 that due to the strong confining nature of QCD, perturbative techniques often fail at long ranges since $\alpha_s > 1$. To address this, QCDSR is typically used to compute nonperturbative TFFs with input DAs obtained from expansions in terms of Gegenbauer polynomials.

The moments of two-particle DAs in the QCDSR approach are given by [8]

$$\langle \xi_{\parallel,\perp}^n \rangle = \int dx \xi^n \phi_{\parallel,\perp}(x, \mu), \quad (4.1)$$

where $\xi = 2x - 1$ and μ is the renormalization scale factor. The moments are deter-

mined at a starting scale of $\mu = 1$ GeV. The DA is normalized such that,

$$\int \phi_{\parallel,\perp}(x, \mu) dx = 1. \quad (4.2)$$

In the standard sum rules approach, only the first two terms in the expansion are non-zero [1]. Therefore, the DAs are expanded in terms of truncated Gegenbauer polynomials:

$$\phi_{\parallel,\perp}(x, u) = 6x\bar{x} \left[1 + \sum_{j=1}^2 a_j^{\parallel,\perp}(\mu) C_j^{3/2}(\xi) \right], \quad (4.3)$$

where $C_j^{3/2}$ are the Gegenbauer polynomials and the coefficients $a_j^{\parallel,\perp}(\mu)$ are obtained from the corresponding moments in equation 4.1.

4.2 LCSR

LCSR is a method used to calculate TFFs using DAs traditionally obtained from QCDSR. This process leads to predictions of TFFs that are widely reported in literature. Here, we instead obtain input DA's from hQCD, since other valuable results can be derived using this approach (e.g., parton distribution functions and mass spectra).

For our DAs, we use the LFWF for mesons determined by Brodsky and de Téramond in equation 1.7.

The mass spectra for mesons and baryons provided by hQCD are given by [4]:

$$M^2 = 4\kappa^2 \left(n_T + L + \frac{S}{2} \right) \text{ for mesons,} \quad (4.4)$$

and

$$M^2 = 4\kappa^2 \left(n_T + L + \frac{S}{2} + 1 \right) \text{ for baryons.} \quad (4.5)$$

Where M^2 is the hadron mass squared; $\kappa = 0.54$ GeV is the AdS/QCD scale; and n_T is the radial quantum number; and L and S are the familiar quantum numbers. These spectra predict that the lightest meson bound state with quantum numbers $n_T = L = S = 0$, is massless [6], in contrast to the spectrum produced by the 't Hooft framework. Using the 't Hooft equation allows us to find the longitudinal mass contribution independently as an eigenvalue, meaning it does not predict massless mesons.

This failure to predict massive mesons for certain quantum numbers is one many drawbacks which motivate the use of the 't Hooft equation in the solution of the LF Schrödinger equation.

To find the $B_s \rightarrow \phi$ TFF using LCSR, we start with the meson wave function (equation 1.2) found from the QCD Lagrangian (equation 1.1).

The longitudinal mode $X(x)$ is determined through an exact mapping of the pion electromagnetic form factors in anti-de Sitter (AdS) and physical spacetime [5], yielding

$$X(x) = \sqrt{x(1-x)}. \quad (4.6)$$

The transverse mode of equation 1.2 is augmented through Brodsky and de Téramond's prescription in [12], which introduces a polarization-dependent normalization constant, N_λ :

$$\Psi_\lambda^\phi(x, \zeta) = \mathcal{N}_\lambda \sqrt{x\bar{x}} \exp \left[-\frac{\kappa^2 \zeta^2}{2} \right] \exp \left[-\frac{m_q^2}{2\kappa^2 x\bar{x}} \right] \quad (4.7)$$

Recall that the form of the longitudinal mode $X(x) = \sqrt{x\bar{x}}$ relies on the assumption that quarks are massless. However, we have accounted for non-zero quark masses for equal mass cases (i.e., when $m_q = m_{\bar{q}}$) by appending the term $\exp\left[-\frac{m_q^2}{2\kappa^2 x\bar{x}}\right]$, in accordance with the BdT prescription. Furthermore, to account for the quark's spin, we include spin-structure [6] and obtain the light-front vector meson wave functions for the ϕ meson:

$$\Psi_{h,\bar{h}}^{\phi,L}(x,r) = \frac{1}{2}\delta_{h,\bar{h}} \left[1 + \frac{m_q^2 - \nabla_r^2}{x\bar{x}M_\phi} \right] \Psi_L^\phi(x,\zeta) \quad (4.8)$$

for longitudinal polarization, and

$$\Psi_{h,\bar{h}}^{\phi,T}(x,r) = \pm \left[ie^{\pm i\theta r} (x\delta_{h\pm,\bar{h}\mp} - \bar{x}\delta_{h\mp,\bar{h}\pm})\partial_r + m_q\delta_{h\pm,\bar{h}\pm} \right] \frac{\Psi_T^\phi(x,\zeta)}{2x\bar{x}} \quad (4.9)$$

for transverse polarization, where h and \bar{h} are the helicities of the quark and anti-quark, respectively.

We can now use the method prescribed by Ahmady et. al. in [5] to find the relevant distribution amplitudes needed for the $B_s \rightarrow \phi$ TFFs. The relevant twist-2 DAs are given by

$$\phi^\parallel(x) = \frac{1}{f_V^\parallel} \sqrt{\frac{N_c}{\pi}} \int_0^\infty dr \mu J_1(\mu r) \left[1 + \frac{m_{\bar{q}}m_q - \nabla_r^2}{M^2 x\bar{x}} \right] \Psi_L(x,r) \quad (4.10)$$

for the longitudinal DA, and

$$\phi^\perp(x) = \frac{1}{f_V^\perp} \sqrt{\frac{N_c}{2\pi}} \int_0^\infty dr \mu J_1(\mu r) [m_q - x(m_q - m_{\bar{q}})] \frac{\Psi_T(x,r)}{x\bar{x}}, \quad (4.11)$$

for the transverse DA. Here, f_V^\parallel and f_V^\perp are the longitudinal and transverse coupling constants, respectively, from [5]. Both DAs are normalized according to equation 4.2.

Our last prerequisites for computing the seven TFFs are the twist-3 DAs, which

are computed from the LFWF [2]:

$$g_V^{\perp(v)}(x) = \frac{N_c}{2\pi f_V^{\parallel} M} \int_0^\infty dr \mu J_1(\mu r) [(m_q - x(m_q - m_{\bar{q}}))^2 - (x^2 + \bar{x}^2)\nabla^2] \frac{\Psi_T(r, x)}{x^2 \bar{x}^2} \quad (4.12)$$

for the vector DA, and

$$\frac{df^{\perp(a)V}}{dx}(x) = \frac{\sqrt{2}N_c}{\pi \tilde{f}_V M} \int_0^\infty dr \mu J_1(\mu r) [(1 - 2x)(m_q^2 - \nabla^2) + x^2(m_q + m_{\bar{q}})(m_q - m_{\bar{q}})] \frac{\Psi_T(r, x)}{x^2 \bar{x}^2} \quad (4.13)$$

for the axial DA, where

$$\tilde{f}_V = f_V^{\parallel} - f_V^{\perp} \left(\frac{m_q - m_{\bar{q}}}{m_V} \right).$$

Since the axial DA is given in terms of a derivative, it must be computed numerically.

The vector and axial TFFs are defined by [18]:

$$\begin{aligned} \langle \phi(k, \epsilon) | \bar{s} \gamma^\mu (1 - \gamma^5) b | B_s(p) \rangle &= \frac{2iV(q^2)}{m_{B_s} + m_\phi} \epsilon^{\mu\nu\rho\sigma} \epsilon_\nu^* k_\rho p_\sigma - 2m_\phi A_0(q^2) \frac{\epsilon^* q}{q^2} q^\mu \\ &\quad - (m_{B_s} + m_\phi) A_1(q^2) \left(\epsilon^{\mu*} - \frac{e^* q}{q^2} q^\mu \right) \\ &\quad + A_2(q^2) \frac{\epsilon^* q}{m_{B_s} + m_\phi} \left[(p + k)^\mu - \frac{m_{B_s}^2 - m_\phi^2}{q^2} q^\mu \right] \end{aligned} \quad (4.14)$$

where ϵ is the polarization 4-vector of the vector meson V , and $q = p - k$ is the

4-momentum transfer. The three tensor form factors are similarly defined as [18],

$$\begin{aligned}
q_\nu \langle \phi(k, \varepsilon) | \bar{s} \sigma^{\mu\nu} (1 - \gamma^5) b | B_s(p) \rangle = & 2T_1(q^2) \epsilon^{\mu\nu\rho\sigma} \varepsilon_\nu^* p_\rho k_\sigma \\
& - iT_2(q^2) [(\varepsilon^* q)(p+k)_\mu - \varepsilon_\mu^* (m_{B_s}^2 - m_\phi^2)] \\
& - iT_3(q^2) (\varepsilon^* q) \left[\frac{q^2}{m_{B_s}^2 - m_\phi^2} (p+k)_\mu - q_\mu \right]. \quad (4.15)
\end{aligned}$$

At long last, we can finally compute the TFFs! There are seven $B_s \rightarrow \phi$ TFFs: One vector, three axial, and three tensor. According to LCSR, at $q^2 = 0$, they are given as [18]:

$$\begin{aligned}
V(0) = & \frac{m_{B_s} + m_\phi}{2} \frac{m_b + m_s}{f_{B_s} m_{B_s}^2} \exp\left(\frac{m_{B_s}^2}{M_{B_s}^2}\right) \int_\delta^1 du \exp\left(\frac{-m_b^2 + p^2 u \bar{u}}{u M_{B_s}^2}\right) \\
& \times \left(\frac{m_b m_\phi f_\phi^\parallel g_\phi^{\perp(a)}(u)}{2u^2 M_{B_s}^2} + \frac{f_\phi^\perp \phi^\perp(u)}{u} \right) \quad (4.16)
\end{aligned}$$

for the vector form factor,

$$\begin{aligned}
A_1(0) = & \frac{1}{m_{B_s} + m_\phi} \frac{m_b + m_s}{f_{B_s} m_{B_s}^2} \exp\left(\frac{m_{B_s}^2}{M_{B_s}^2}\right) \int_\delta^1 du \exp\left(\frac{-m_b^2 + p^2 u \bar{u}}{u M_{B_s}^2}\right) \\
& \times \left(\frac{m_b m_\phi f_\phi^\parallel g_\phi^{\perp(v)}(u)}{u} + \frac{(m_b^2 + u^2 m_\phi^2) f_\phi^\perp \phi^\perp(u)}{2u^2} \right), \\
A_2(0) = & - \frac{(m_{B_s} + m_\phi)(m_b + m_s)}{f_{B_s} m_{B_s}^2} \exp\left(\frac{m_{B_s}^2}{M_{B_s}^2}\right) \int_\delta^1 du \exp\left(\frac{-m_b^2 + p^2 u \bar{u}}{u M_{B_s}^2}\right) \\
& \times \left(- \frac{m_b m_\phi f_\phi^\parallel \Phi_\parallel(u)}{u^2 M_{B_s}^2} - \frac{f_\phi^\perp \phi^\perp(u)}{2u} \right), \\
A_0(0) = & \left(\frac{m_{B_s} + m_\phi}{2m_\phi} \right) A_1(0) + \left(\frac{m_\phi - m_{B_s}}{2m_\phi} \right) A_2(0) \quad (4.17)
\end{aligned}$$

for the three axial TFFs, and finally,

$$\begin{aligned}
T_1(0) &= \frac{m_b + m_s}{2f_{B_s} m_{B_s}^2} \exp\left(\frac{m_{B_s}^2}{M_{B_s}^2}\right) \int_{\delta}^1 du \exp\left(\frac{-m_b^2 + p^2 u \bar{u}}{u M_{B_s}^2}\right) \left[m_b f_{\phi}^{\perp} \phi^{\perp}(u) \right. \\
&\quad \left. + f_{\phi}^{\parallel} m_{\phi} \left(\Phi_{\parallel}(u) + u g_{\phi}^{\perp(v)}(u) + \frac{g_{\phi}^{\perp(a)}(u)}{4} + \frac{(m_b^2 - p^2 u^2) g_{\phi}^{\perp(a)}(u)}{4u M_{B_s}^2} \right) \right] \\
T_2(0) &= \frac{1}{m_{B_s}^2 - m_{\phi}^2} \frac{m_b + m_s}{f_{B_s} m_{B_s}^2} \exp\left(\frac{m_{B_s}^2}{M_{B_s}^2}\right) \int_{\delta}^1 du \exp\left(\frac{-m_b^2 + p^2 u \bar{u}}{u M_{B_s}^2}\right) \\
&\quad \times \left(\frac{m_b f_{\phi}^{\perp} \phi^{\perp}(u)}{2u} (m_b^2 - p^2 u^2) + f_{\phi}^{\parallel} m_{\phi} \right. \\
&\quad \left. \times \left[\frac{m_b^2 - p^2 u^2}{2u} \left(\Phi_{\parallel}(u) + u g_{\phi}^{\perp(v)}(u) + \frac{(m_b^2 - p^2 u^2) g_{\phi}^{\perp(a)}(u)}{4u M_{B_s}^2} \right) \right] \right), \\
T_3(0) &= \frac{1}{m_{B_s}^2 - m_{\phi}^2} \frac{m_b + m_s}{f_{B_s} m_{B_s}^2} \exp\left(\frac{m_{B_s}^2}{M_{B_s}^2}\right) \int_{\delta}^1 du \exp\left(\frac{-m_b^2 + p^2 u \bar{u}}{u M_{B_s}^2}\right) \\
&\quad \times \left\{ m_{\phi} f_{\phi}^{\parallel} \left[\frac{g_{\phi}^{\perp(a)}(u)}{4} + \frac{(m_b^2 - p^2 u^2) g_{\phi}^{\perp(a)}(u)}{4u M_{B_s}^2} \right] \right. \\
&\quad - 2m_{\phi} f_{\phi}^{\parallel} \left[\frac{g_{\phi}^{\perp(v)}(u)(2-u)}{2} - \frac{p^2 g_{\phi}^{\perp(a)}(u)}{2M_{B_s}^2} \right] \\
&\quad \left. + 2m_{\phi} f_{\phi}^{\parallel} \left[\frac{\Phi_{\parallel}(u)}{u M_{B_s}^2} \left(\frac{m_b^2 - p^2 u^2}{u} - M_{B_s}^2 + \frac{u M_{B_s}^2}{2} \right) \right] + m_b f_{\phi}^{\perp} \phi^{\perp}(u) \right\}, \quad (4.18)
\end{aligned}$$

for the three tensor TFFs. The lower integration limit

$$\delta = \frac{m_b^2 - q^2}{s_0^B - q^2}$$

is dependent on the continuum threshold value $s_0^B = 36 \text{ GeV}^2$ [1]. The function $\Phi_{\parallel}(u)$

is also given by [1]

$$\Phi_{\parallel}(u) = \frac{1}{2} \left[(1-u) \int_0^u dz \frac{\phi_{\parallel}(z)}{1-z} - u \int_u^1 \frac{\phi_{\parallel}(z)}{z} \right].$$

Other parameters used in the formulas for the TFFs include the Borel parameter $M_{B_s}^2 = 8 \text{ GeV}^2$, the bottom quark mass $m_b = 4.84 \text{ GeV}$, the B meson mass $m_{B_s} = 5.37 \text{ GeV}$ and the decay constant $f_{B_s} = 224 \text{ GeV}$ [16].

Now that we've defined our TFFs, there is one last obstacle we must surmount before we can calculate them. Namely, since LCSR is only valid in the low-to-intermediate momentum transfer regime, each form factor must be extrapolated to high q^2 using a two-parameter fit of the form

$$F(q^2) = \frac{F(0)}{1 - a \left(\frac{q^2}{m_{B_s}^2} \right) + b \left(\frac{q^4}{m_{B_s}^4} \right)} \quad (4.19)$$

to the LCSR predictions as well as form factor values obtained from lattice QCD which are only valid at high momentum transfer [5]. Here, a and b are the free parameters.

Inherent in the LCSR approach are several sources of uncertainty, some of which include uncertainty from the Borel parameter, the continuum threshold, and the above two-parameter fit. However, since LCSR is used to find TFFs with input DAs from both QCDSR and hQCD, these sources of uncertainty may be effectively ignored.

	V	A_0	A_1	A_2	T_1	T_2	T_3
F(0) (hQCD)	0.26 ± 0.2	0.15 ± 0.03	0.19 ± 0.02	0.21 ± 0.01	0.21 ± 0.03	0.22 ± 0.01	0.16 ± 0.01
F(0) (QCDSR)	0.33 ± 0.01	0.27 ± 0.01	0.26 ± 0.01	0.26 ± 0.01	0.27 ± 0.01	0.28 ± 0.01	0.18 ± 0.01

Table 4.1: Predictions for the seven $B_s \rightarrow \phi$ form factors at $q^2 = 0$ using DAs obtained from QCDSR and hQCD. The uncertainty in the form factors comes from variation in strange quark mass (m_s) and the confinement scale (κ).

The values for the seven TFFs at $q^2 = 0$ are given in Table 4.1. Note that LCSR

consistently predicts lower values than QCDSR.

TFFs can be used to find a range of other important observables which serve as important tests of the SM. For example, Ahmady et. al. use the above TFFs to calculate the differential branching ratio for the $B_s \rightarrow \phi \mu^+ \mu^-$ decay. The results generated using DAs obtained from hQCD (shown in Figure 4.1) are in better agreement with the latest LHCb data than the prediction found using QCDSR DAs [5]. It

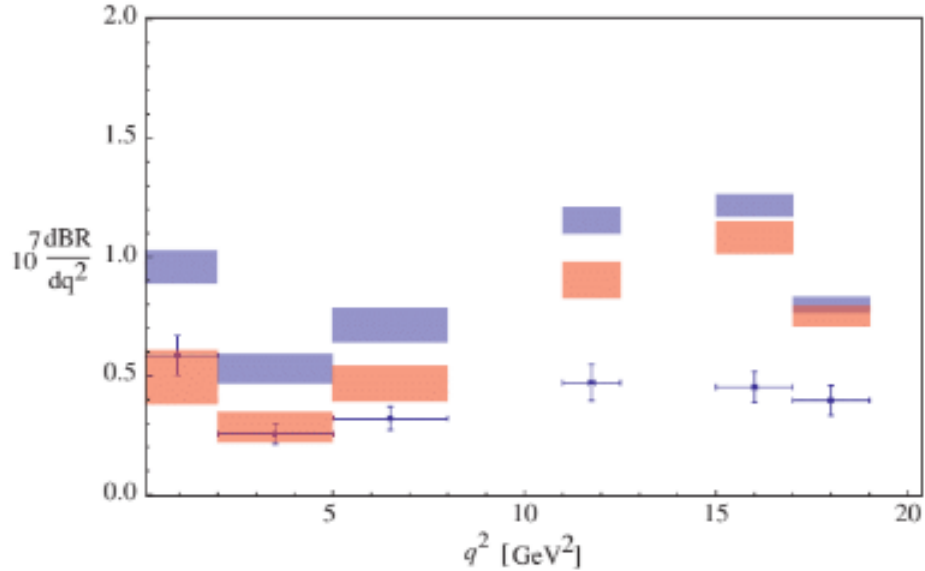


Figure 4.1: The differential branching ratio for $B_s \rightarrow \phi \mu^+ \mu^-$ as predicted by hQCD (red rectangles) and QCDSR (blue rectangles). The uncertainty widths are due to the form factors. The experimental data points are measured by LHCb [5].

is evident that the differential branching ratio produced using DAs from hQCD is in better agreement with experiment than the prediction obtained using DAs from QCDSR.

TFFs and differential branching ratios are just two examples of values that we can use to compare each of the three approaches to finding input DAs that have been explored in this paper: QCDSR, hQCD using the BdT prescription, and hQCD using longitudinal dynamics derived from the 't Hooft equation.

Currently, data found using the latter approach is preliminary and scarce, but we

will see in the following section that there is ample room for investigation to this end. It nonetheless remains unclear if important quantities like the differential branching ratio produced using longitudinal dynamics derived from the 't Hooft Equation will yield better agreement with experiment than the prediction using hQCD and the BdT prescription.

It is therefore prudent for future investigations into this novel approach to compare TFFs and differential branching ratios to data obtained in other literature like ref. [5].

4.3 $B \rightarrow \pi$ Form Factors Using Overlap Formulas

There are two ways we can go about computing TFFs using the tools developed thus far. One way is to use LCSR in tandem with equations 4.16, 4.17, and 4.18 to analytically solve for the TFFs. However, we can also calculate them directly using overlap formulas in terms of the initial LFWFs of the initial B-meson state and the final phase state [4].

To begin, we extract f^+ from the transition matrix element in the Drell-Yan frame ($q^+ = 0$), given by [7]

$$\langle \pi(P_\pi) | \bar{q}_d \gamma_\mu (1 - \gamma_5) q_b | B(P_B) \rangle = f^+(q^2) (P_B + P_\pi)_\mu + f^-(q^2) (P_B - P_\pi)_\mu, \quad (4.20)$$

where P_B and P_π are the four-momentum vectors of the B and π mesons, respectively; and $q^2 = (P_B - P_\pi)^2$ is the 4-momentum transfer.

Choosing $\mu = +$ and noting that $P_B^+ = P_\pi^+$ gives rise to the following equation for $f^+(q^2)$ when dynamical spin effects are taken into account for the spin-improved

wave functions given by equation 1.11 ($B > 0$):

$$f^+(q^2) = \int \frac{dx d^2\mathbf{k}}{16\pi^3} [\Psi_{\downarrow\uparrow}^{\pi*}(x, \mathbf{k} + \bar{x}\mathbf{q})\Psi_{\downarrow\uparrow}^B(x, \mathbf{k}) + \Psi_{\downarrow\downarrow}^{\pi*}(x, \mathbf{k} + \bar{x}\mathbf{q})\Psi_{\downarrow\downarrow}^B(x, \mathbf{k})], \quad (4.21)$$

where

$$\not\int \frac{d^2\mathbf{k}}{16\pi^3} \Psi_{h,\bar{h}}^{\pi*}(x, \mathbf{k} + \bar{x}\mathbf{q})\Psi_{h,\bar{h}}^B(x, \mathbf{k}) = -\tilde{\mathcal{N}}\bar{x}\mathbf{q} \exp\left(-\frac{(q_{\perp}\bar{x}^2) + 4(\bar{x}m_q^2 + xm_{\bar{q}}^2)}{4\kappa^2x\bar{x}}\mathcal{M}(x)\right) \quad (4.22)$$

and

$$\not\int \frac{d^2\mathbf{k}}{16\pi^3} \Psi_{h,\bar{h}}^{\pi*}(x, \mathbf{k} - \bar{x}\mathbf{q})\Psi_{h,\bar{h}}^B(x, \mathbf{k}) = \tilde{\mathcal{N}}\bar{x}\mathbf{q} \exp\left(-\frac{(q_{\perp}x^2) + 4(\bar{x}m_q^2 + xm_{\bar{q}}^2)}{4\kappa^2x\bar{x}}\mathcal{M}(x)\right). \quad (4.23)$$

Additionally, $\tilde{\mathcal{N}}$ is a normalization factor, and

$$\mathcal{M}(x) = \frac{1}{x\bar{x}} \left(\frac{M_B}{2} + B \left(\frac{\bar{x}m_q + xm_{\bar{q}}}{x\bar{x}} \right) \right),$$

where the shorthand notation $\not\int \equiv \sum_{h,\bar{h}} f$ is used.

However, at $q^2 = 0$, both of the above equations reduce to

$$\not\int \frac{d^2\mathbf{k}}{16\pi^3} \Psi_{h,\bar{h}}^{\pi*}(x, \mathbf{k})\Psi_{h,\bar{h}}^B(x, \mathbf{k}). \quad (4.24)$$

If we do not take into account dynamical spin effects ($B = 0$), the sum over all helicities simply yields a factor of 4 multiplied by the product of both wave functions, rather than the expression we see in equation 4.21. Therefore, for $f^+(0)$ at $B = 0$,

we have

$$f^+(0) = \int \frac{dx d^2\mathbf{k}}{8\pi^3} \Psi^{\pi^*}(x, \mathbf{k}) \Psi^B(x, \mathbf{k}). \quad (4.25)$$

Obtaining form factors for decays such as $B \rightarrow \pi l^+ l^-$ has been one of the primary goals of this investigation, as these results could speak to the viability of using longitudinal dynamics obtained from the 't Hooft equation in hQCD. While not much has been accomplished to this end, preliminary results were obtained for f^+ using the above overlap formulas.

It was found that, using these new dynamics, $f_{B \rightarrow \pi l^+ l^-}^+(q^2 = 0) = 1.42$. This value differs significantly from what has been reported in other literature and warrants much further investigation. For instance, Ball and Zwicky report the same form factor to be 0.250, 0.258, 0.263, and 0.274 for different sets of parameters (e.g., b quark mass, meson mass, etc.) using LCSR with input DA's from QCDSR [9].

Nonetheless, there are several advantages to using the above overlap formulas for computing TFFs as an alternative to LCSR. Primarily, meson LFWFs are more informative than DAs, so it is convenient to use an approach that can directly compute TFFs from LFWFs. In addition, TFFs found via LCSR are only valid at low-to-intermediate momentum transfers, and must be extrapolated using lattice data in order to make predictions over the full range of q^2 . This, as well as other sources of uncertainty inherent in LCSR, make the overlap formulas the preferable approach for computing TFFs.

However, using a solution to the 't Hooft equation to find the longitudinal mode presents a new problem for the B meson LFWF, and thus a problem for the overlap formulas (hence why particular emphasis has been placed on the $B = 0$ case). Namely, the inclusion of spin effects can cause unpredictable or non-physical behaviour in the parton distribution function and observables for heavy systems with this new

longitudinal mode. Some of these issues include parton distribution functions which diverge at their endpoints, or decay constants and charge radii which deviate several orders of magnitude from their experimental values.

This restricts any predictions for most systems to only use $B = 0$. In contrast, past literature has included dynamical spin effects ($B \geq 0$) as per the BdT prescription in the prediction of various observables and attained excellent agreement with experiment without incorporating a solution to the 't Hooft equation [4, 6]. Since the above overlap formulas are also sensitive to the dynamical spin parameter, we lose some leniency in our direct calculations of TFFs.

This incompatibility with the BdT prescription is currently not well-understood and warrants further investigation.

We are therefore left with two options, each with their own drawbacks: We can use hQCD with $X(x) = \sqrt{x\bar{x}}$ and not account for longitudinal mass contributions, or we can use longitudinal dynamics derived from the 't Hooft equation and not account for dynamical spin effects.

Chapter 5

Results

5.1 Meson Masses and Distribution Amplitudes

Using the 't Hooft equation to incorporate longitudinal mass contributions into the mass spectrum for various mesons, we calculated their total masses as a function of the current quark masses, 't Hooft coupling, and number of expansion terms. The 't Hooft couplings corresponding to particular mesons are given in Table 5.1 [3].

Mesons	g	$m_{u/d}$	m_s	m_c	m_b
Light	0.128	0.046	0.357	-	-
Heavy-light	0.680	0.046	0.357	1.370	4.640
Heavy-heavy	0.523	-	-	1.370	4.640

Table 5.1: Quark masses and 't Hooft couplings in GeV. The confinement scale is fixed at $\kappa = 0.523$ GeV for all mesons.

The calculated masses for various mesons are given in Figure 5.1. Notice that, as expected, the mass values do not converge until a sufficiently large number of terms is reached (especially for heavier mesons). In most cases, this is around $r = 3$ terms. However, we've seen that such a small expansions nonetheless lead to inaccurate longitudinal dynamics in heavy systems, necessitating larger expansions (up to $r = 19$ terms for heavy mesons like the η_b).

The meson masses are determined by the stability plateau, where the predicted mass changes minimally between successive terms. Also note that the parameters used for the red points and the blue points are different: The red points (coming from solutions to the 't Hooft Equation) use the parameters from Table 5.1. The

blue points use effective light quark masses derived from the pion and kaon masses and the effective charm quark mass obtained from the η_c using equation 3.16 [15]. No blue points appear for the B or η_b in Figure 5.1 owing to the fact that similar analysis was not done for the b quark in the other literature [15].

Another important result that was calculated are the Regge slopes for the pion and its excited states, which is shown in Figure 5.2. The solutions to the 't Hooft equation were used to compute the longitudinal mass contribution for each system. The agreement with observation is good, and comparable to the level of accuracy achieved by the BdT prescription [13].

With the exception of non-radially excited states, it is emphasized that the position and slope of the Regge trajectory for the pion is sensitive to κ and g . Ahmady et. al. [3] used this observation and Regge slopes for other mesons to determine that the universality of κ across the full spectrum of pseudoscalar and vector mesons is non-trivial.

A point of interest emerged from the phenomenology of this approach: In spite of the 't Hooft equation's success at predicting certain meson masses, are there quark mass/coupling constant combinations that produce greater agreement for meson masses with the observed values? This was explored at length for systems of varying meson masses, and the results of the investigation are found in Figures 5.3 to 5.6. The darker regions in each plot represent areas of greater agreement (lower fractional difference).

In general, it seems that for the acceptable quark masses, the best agreement is achieved for a stronger coupling than that listed in Table 5.1. For the heaviest systems - namely the η_b and η_c - we see good agreement for a very wide range of coupling constants corresponding to a small ranges of quark masses. This indicates that the predicted meson mass becomes less sensitive to g as the mass of the $q\bar{q}$ pair

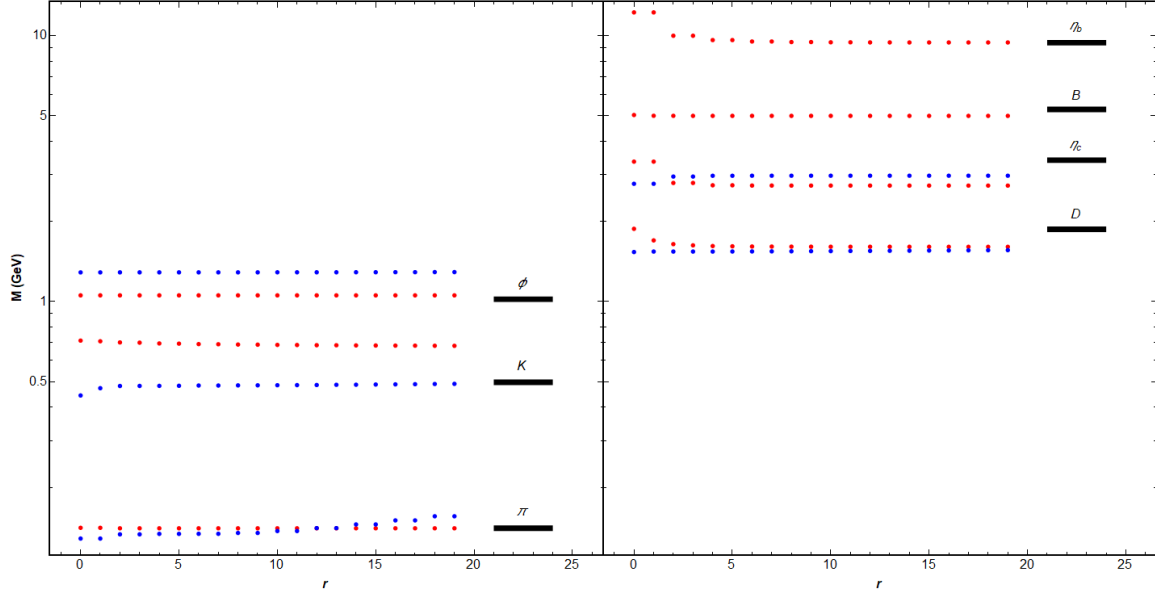


Figure 5.1: Predictions for various ground state meson mass values using an increasing number of expansion coefficients, r , in the numerical solution to the 't Hooft equation (red) and in the expansion from Brodsky and de Téramond given by equation 3.16 (blue). The horizontal black lines are the observed masses.

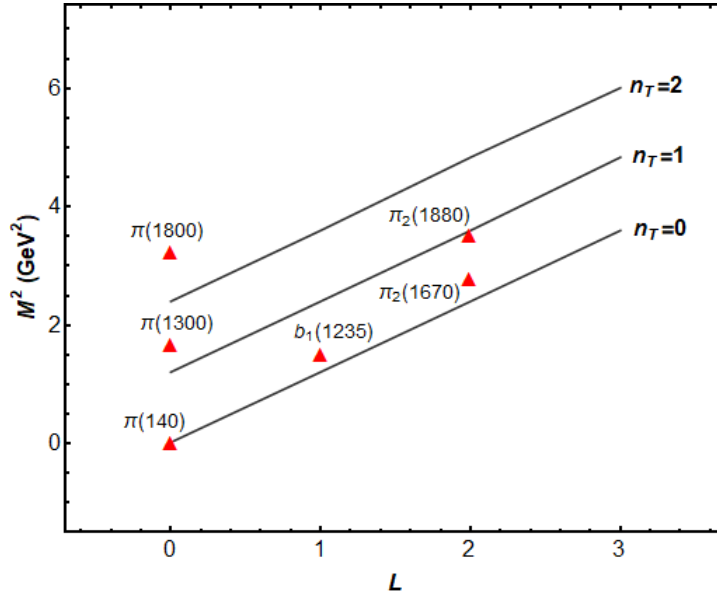


Figure 5.2: Predictions for Regge slopes of the pion and its orbitally/radially excited states up to $n_T = 2$, using the 't Hooft equation to predict the square of the longitudinal mass.

increases, as we would expect.

This investigation was also motivated by a problem encountered in the computation of meson parton distribution functions (pdfs): From the solution to the holographic Schrödinger equation (1.3), we know that the LF meson wave function is of the form

$$\Psi(x, \zeta^2) = NX(x) \exp\left(-\frac{\kappa^2 \zeta^2}{2}\right).$$

Substituting $\zeta^2 = x(1-x)b^2$,

$$\Psi(x, b) = NX(x) \exp\left(-\frac{\kappa^2 x(1-x)b^2}{2}\right)$$

The pdf for a meson with this wave function is given by [6],

$$f(x) = \int d^2b |\Psi(x, b)|^2,$$

which evaluates to,

$$f(x) = \frac{2\pi NX^2(x)}{2\kappa^2 x(1-x)}.$$

This means that the functional behaviour of the meson pdf is

$$f(x) \propto \frac{X^2(x)}{x(1-x)}, \tag{5.1}$$

suggesting that if the longitudinal mode features $\beta_1 = \beta_2 < 0.5$, then the pdf will be divergent at its endpoints! Since this is clearly nonphysical (a particle cannot have an *infinite* probability of existing anywhere), it was determined that this could in part be caused by the input masses or couplings.

To investigate which inputs this occurred for, a nonlinear fit to the form x^{β_1} was performed on the longitudinal modes corresponding to each combination of quark masses and coupling constants. The β_1 values near the endpoint $x = 0$ were determined for each combination. As pictured in Figure 5.3, it was found that this requirement restricted the allowable combinations of quark masses and coupling constants to the bottom-left half of the plot (for small quark masses and 't Hooft couplings).

Strong emphasis was placed on the endpoint behaviour of the longitudinal mode because the transcendental equation (equation 3.3) - which determines the values of β_1 and β_2 - is derived from analysis of endpoint behaviour. This, along with the symmetry of the pion longitudinal mode, is why a fit to the form x^{β_1} was sufficient to determine the functional behaviour.

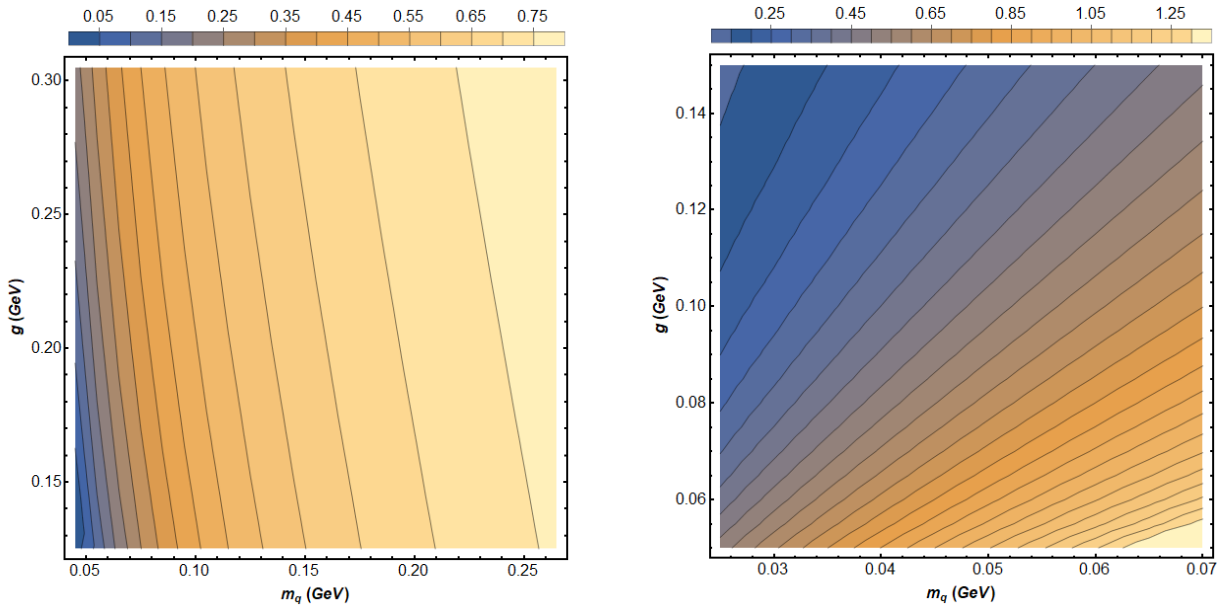


Figure 5.3: Predictions for the light quark mass and coupling constant combination that will produce the greatest agreement (lowest fractional difference) with experimental pion mass values (left) and our predictions for the light quark mass and coupling constant combination which will produce values of $\beta \geq 0.5$ in the ansatz $X(x) = \mathcal{N}x^{\beta_1}(1-x)^{\beta_2}$, where \mathcal{N} is a normalization factor (right). We vary both light quark masses.

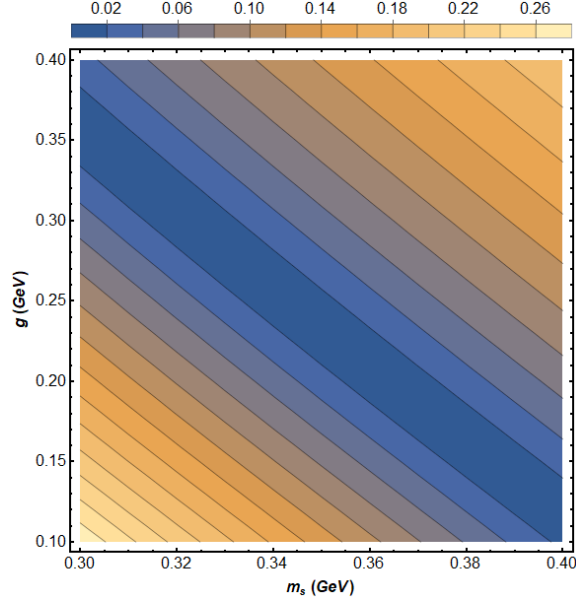


Figure 5.4: Predictions for the strange quark mass and coupling constant combination that will produce the greatest agreement with experimental kaon mass values . We hold the light quark mass fixed at $m_q = 0.046$ GeV while varying the strange quark mass.

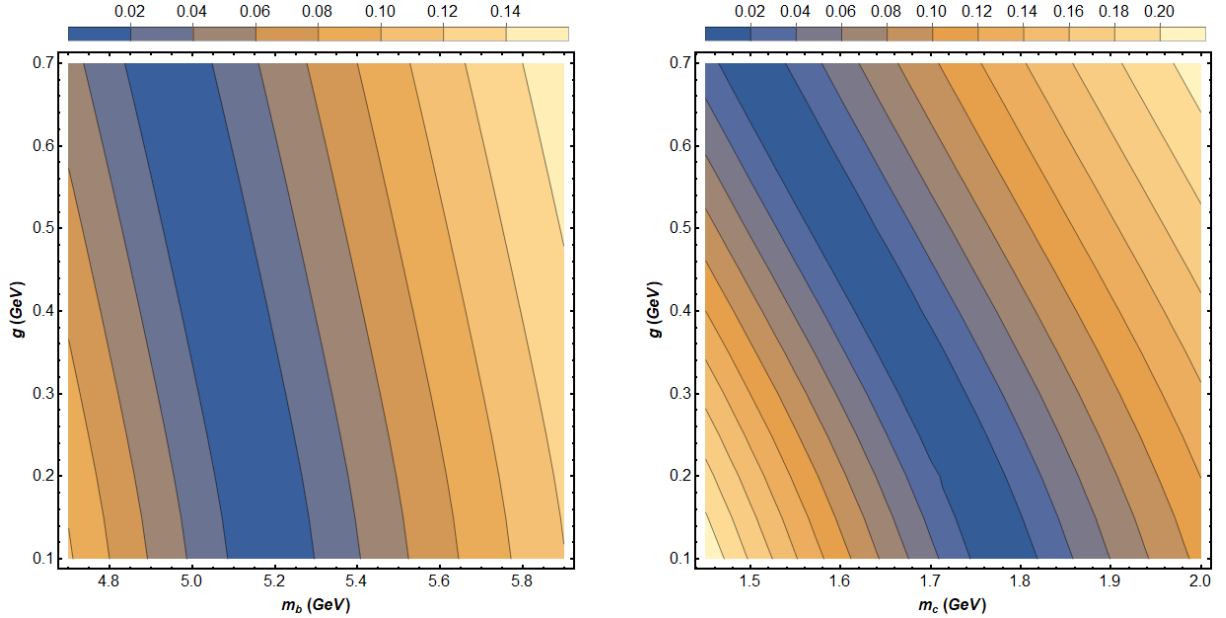


Figure 5.5: Predictions for the heavy quark mass and coupling constant combination that will produce the greatest agreement with experimental B mass values (left) and experimental D mass values (right). We hold the light quark mass fixed at $m_q = 0.046$ GeV while varying the bottom and charm quark masses.

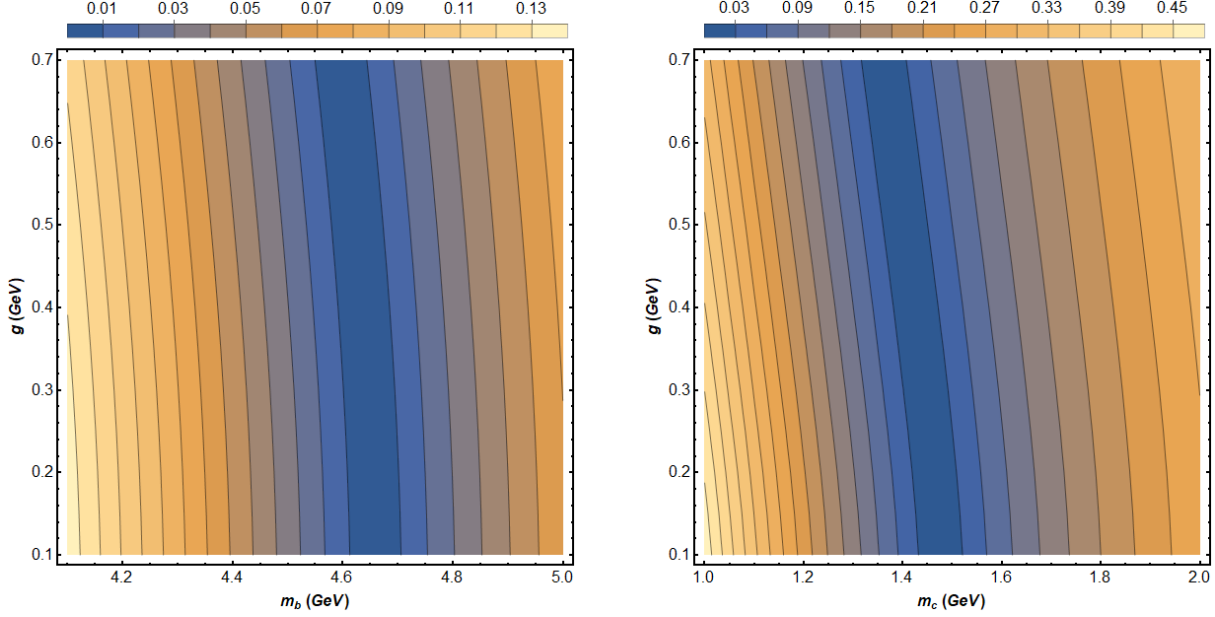


Figure 5.6: Predictions for the heavy quark masses and coupling constant combination that will produce the greatest agreement with experimental bottomonium (η_b) mass values (left) and charmonium (η_c) mass values (right). We vary both bottom quark masses and charm quark masses in each case.

Using the BdT approach, the pdfs in Figures 5.7 to 5.11 assume the form,

$$\Psi(x, \zeta) = N \sqrt{x(1-x)} X(x) \exp\left(-\frac{\kappa^2 \zeta^2}{2}\right). \quad (5.2)$$

Figures 5.7 to 5.11 feature a comparison of the longitudinal modes and pdfs obtained from both methods detailed in Section 3.1. Both approaches generally agree well (especially for heavier systems), with some exceptions.

Namely, the longitudinal mode and pdf for the pion predicted by BdT is relatively flat near $x = 0.5$. This is likely due to the explicit incorporation of the BdT form of the longitudinal mode (equation 1.7) in the solution for the expansion coefficients in equation 3.16. In contrast, the 't Hooft solution features a form with a stronger resemblance to the ansatz $X(x) = \sqrt{x(1-x)}$.

However, the most important point of comparison for both the DAs and pdfs

is their endpoint behaviour, as (according to the transcendental equation given by equation 3.3) β_1 and β_2 are sensitive to it. It seems that the pdfs found from 't Hooft potential and BdT potential boast good agreement near their endpoints.

Note that none of the following pdfs include dynamical spin effects ($B = 0$).

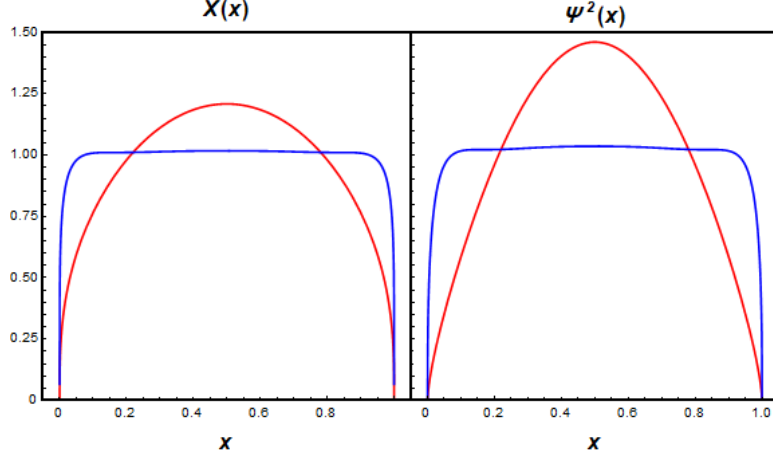


Figure 5.7: Pion longitudinal mode (left) and pdf (right) from a numerical solution to the 't Hooft equation in red, and the solution from Brodsky's analytical method in blue. The following parameters were used: $m_q = m_{\bar{q}} = 0.046$ GeV, $g = 0.128$ GeV, $\beta_1 = \beta_2 = 0.34$, and a matrix size of $r = s = 7$.

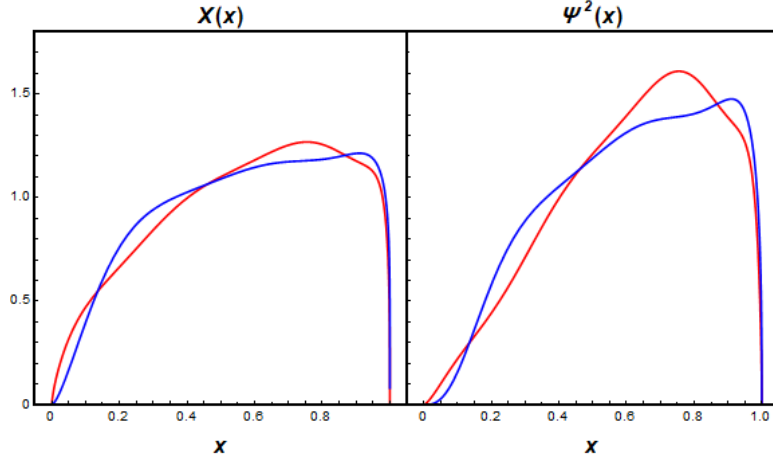


Figure 5.8: Kaon longitudinal mode (left) and pdf (right) from a numerical solution to the 't Hooft equation in red, and the solution from Brodsky's analytical method in blue. The following parameters were used: $m_q = 0.357$ GeV, $m_{\bar{q}} = 0.046$ GeV, $g = 0.680$ GeV, $\beta_1 = 0.7$, $\beta_2 = 0.35$, and a matrix size of $r = s = 9$.

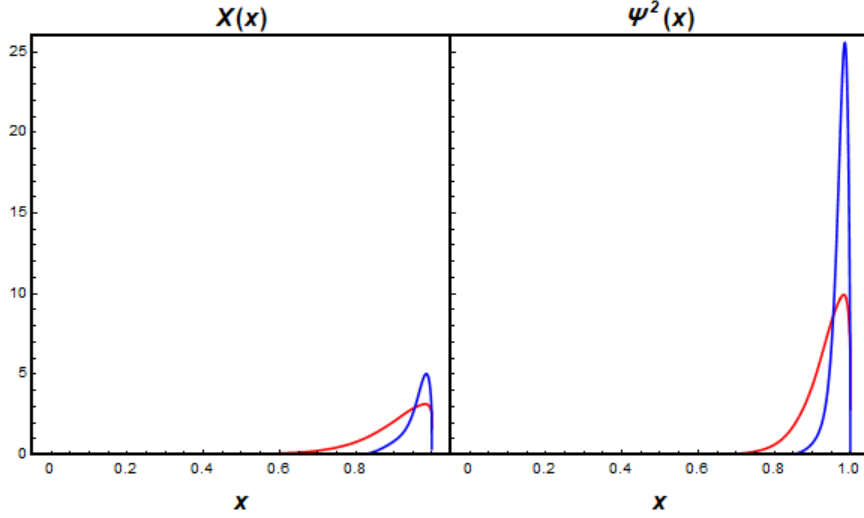


Figure 5.9: B longitudinal mode (left) and pdf (right) from a numerical solution to the 't Hooft equation in red, and the solution from Brodsky's analytical method in blue. The following parameters were used: $m_q = 4.64$ GeV, $m_{\bar{q}} = 0.046$ GeV, $g = 0.680$ GeV, $\beta_1 = 10$, $\beta_2 = 0.04$, and a matrix size of $r = s = 16$.

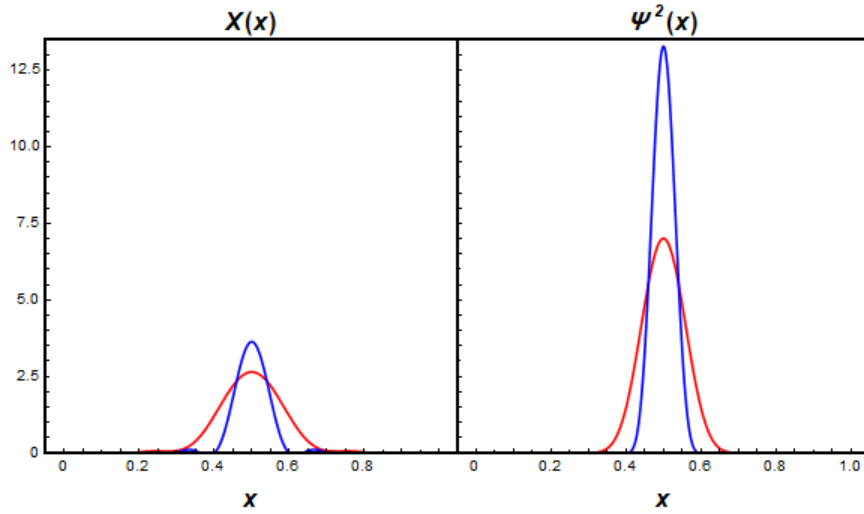


Figure 5.10: Bottomonium longitudinal mode (left) and pdf (right) from a numerical solution to the 't Hooft equation in red, and the solution from Brodsky's analytical method in blue. The following parameters were used: $m_q = m_{\bar{q}} = 4.64$ GeV, $g = 0.523$ GeV, $\beta_1 = \beta_2 = 0.34$, and a matrix size of $r = s = 16$.

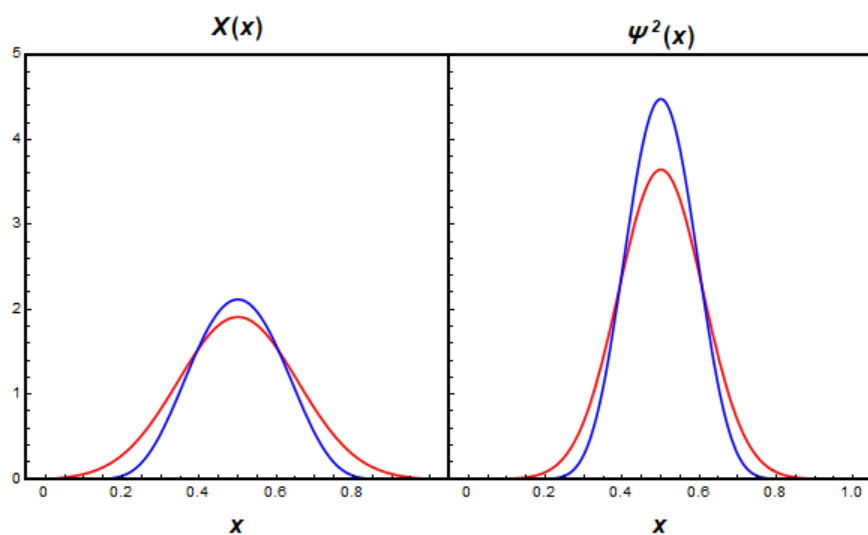


Figure 5.11: Charmonium longitudinal mode (left) and pdf (right) from a numerical solution to the 't Hooft equation in red, and the solution from Brodsky's analytical method in blue. The following parameters were used: $m_q = m_{\bar{q}} = 1.37$ GeV, $g = 0.523$ GeV, $\beta_1 = \beta_2 = 0.34$, and a matrix size of $r = s = 16$.

5.2 Decay Constants and Charge Radii

The primary observables found using this new approach are the decay constants and charge radii. The charge radius quantifies to what degree a meson acts as a point-like particle (making it sensitive to long-distance physics), while the decay constant is sensitive to the wave function at zero transverse separation (making it sensitive to short-distance physics). Therefore, a successful simultaneous description of both observables provides a stringent test for any model of the meson wave function [6].

The decay constant for a pseudoscalar meson with the SIWF from equation 1.11 is given by [6]:

$$f_P(m_f, m_{\bar{f}}, M_P, B) = 2\sqrt{\frac{N_c}{\pi}} \int dx [x\bar{x}M_P + B(xm_f + \bar{x}m_{\bar{f}})] \frac{\Psi^P(x, \zeta)}{x\bar{x}} \Bigg|_{\zeta=0}. \quad (5.3)$$

The root-mean-square EM radius using the same SIWF is given by [6]:

$$\sqrt{\langle r_p^2 \rangle} = \left[\frac{3}{2} \int d^2\mathbf{b} dx [b(1-x)]^2 |\Psi^P(x, \mathbf{b})|^2 \right]^{1/2}. \quad (5.4)$$

Using equations 5.3 and 5.4, we found the decay constants and charge radii for several pseudoscalar mesons as a function of the dynamical spin parameter, given in Tables 5.2 to 5.6.

While Ahmady et. al. observed that the inclusion of dynamical spin effects ($B \gg 1$) improved the accuracy of their predictions using the BdT prescription for the LF meson wave function [6], the same is not true for wave functions found using the 't Hooft equation. The inclusion of any spin effects in the charge radius leads to diverging results and the decay constant moving away from the observed values.

Furthermore, using $B \gg 1$ (numerically, $B = 1000$) produces results drastically different from experiment for ground state pseudoscalar mesons. For pion excited

states, we predict values for the decay constant very close to zero, which agrees with observation. Finally, incorporating spin structure for heavier systems seems to exacerbate the discrepancy between our predictions and observations.

In summary, it seems that in order to obtain good agreement with the observed decay constants and charge radii, dynamical spin effects must be kept to a minimum, if not zero. When $B = 0$, we observe good agreement with experiment for the ground state pion decay constant and charge radius, and for the excited pion decay constants. However, using a pdf that incorporates the longitudinal mode from the 't Hooft equation reliably causes the charge radius to diverge for pseudoscalar mesons.

B	Decay Constant (MeV)	PDG (MeV)	Charge Radius (fm)	PDG (fm)
0	166.391	130.2 ± 1.7	0.694	0.659 ± 0.004
0.01	158.764	-	∞	-
0.05	94.838	-	∞	-
0.1	59.012	-	∞	-
1	15.871	-	∞	-
5	11.718	-	∞	-
10	11.196	-	∞	-
100	10.727	-	∞	-
1000	10.680	-	∞	-

Table 5.2: Predictions for decay constants and charge radii of the ground state pion using the spin-improved wave function and the 't Hooft longitudinal mode and experimental values [16].

B	Decay Constant (MeV)	Charge Radius (fm)
0	3.587	0.978
0.01	1.565	∞
0.05	1.560	∞
0.1	2.223	∞
1	2.813	∞
5	2.864	∞
10	2.870	∞
100	2.876	∞
1000	2.876	∞

Table 5.3: Predictions for decay constants and charge radii of the first excited state pion using the spin-improved wave function and the 't Hooft longitudinal mode.

B	Decay Constant (MeV)	Charge Radius (fm)
0	2.636	1.054
0.01	1.058	∞
0.05	0.970	∞
0.1	1.351	∞
1	1.691	∞
5	1.721	∞
10	1.724	∞
100	1.728	∞
1000	1.728	∞

Table 5.4: Predictions for decay constants and charge radii of the second excited state pion using the spin-improved wave function and the 't Hooft longitudinal mode.

B	Decay Constant (MeV)	PDG (MeV)	Charge Radius (fm)	PDG (fm)
0	114.521	155.6 ± 0.4	0.246	0.560 ± 0.031
0.01	78.664	-	1.67	-
0.05	25.169	-	0.160	-
0.1	15.181	-	0.157	-
1	0	-	0	-
5	0	-	0	-
10	0	-	0	-
100	0	-	0	-
1000	0	-	0	-

Table 5.5: Predictions for decay constants and charge radii of the ground state kaon using the spin-improved wave function and the 't Hooft longitudinal mode and experimental values [16].

B	Decay Constant (MeV)	PDG (MeV)	Charge Radius (fm)	PDG (fm)
0	56.580	190.9 ± 4.1	0.150	-
0.01	1.323	-	0.004	-
0.05	0.362	-	0.001	-
0.1	0.241	-	0.001	-
1	0.133	-	0	-
5	0.124	-	0	-
10	0.123	-	0	-
100	0.121	-	0	-
1000	0.121	-	0	-

Table 5.6: Predictions for decay constants and charge radii of the ground state B using the spin-improved wave function and the 't Hooft longitudinal mode and experimental values [16].

Chapter 6

Discussion and Conclusion

We have found that the mass spectrum produced by the 't Hooft equation yields good agreement with results found using different approaches - namely hQCD augmented using the BdT prescription - and experiment. Furthermore, the longitudinal modes of both approaches produce similar endpoint behaviour, which is vital to the determination of β_1 and β_2 in the ansatz $X(x) = x^{\beta_1}(1-x)^{\beta_2}$.

In addition, it was found that the quark mass and 't Hooft coupling combinations listed in Table 5.1 produce good agreement with observed meson masses in comparison to other (possibly nonphysical) combinations.

In spite of the 't Hooft equation's success at producing an accurate mass spectrum, it is not compatible with other approaches that have seen success in other works. Namely, pdfs produced using the 't Hooft equation fail to accurately predict the decay constants and charge radii when incorporating dynamical spin effects (especially for $B \gg 1$ and for heavy mesons). This is helped somewhat by Brodsky and de Téramond's approach, wherein the pdf is multiplied by a factor of $\sqrt{x(1-x)}$. However, a physical answer for the charge radius is obtained only upon the elimination of dynamical spin effects.

However, inclusion of dynamical spin effects causes the excited pion decay constants to tend towards zero, as we would expect.

Going forward, it would be of great interest to calculate other observables (such as the TFFs for certain decays) using the pdf derived from the 't Hooft potential, and compare them to results obtained using different approaches. Namely, the effective potential adopted by Brodsky and de Téramond in Section 3.4. In addition, more

work needs to be done to understand why incorporating dynamical spin effects in pdfs derived from the 't Hooft potential cause particular observables to diverge.

References

- [1] M. Ahmady, R. Campbell, S. Lord, and R. Sandapen. Predicting the $B \rightarrow K^*$ form factors in light-cone qcd. *Physical Review D*, 89(7), Apr 2014.
- [2] M. Ahmady and R. Sandapen. Predicting the isospin asymmetry in $B \rightarrow K^*\gamma$ using holographic ads/qcd distribution amplitudes for the k^* . *Physical Review D*, 88(1), Jul 2013.
- [3] Mohammad Ahmady, Harleen Dahiya, Satvir Kaur, Chandan Mondal, Ruben Sandapen, and Neetika Sharma. Extending light-front holographic QCD using the 't hooft equation. *Physics Letters B*, 823:136754, dec 2021.
- [4] Mohammad Ahmady, Satvir Kaur, Chandan Mondal, and Ruben Sandapen. Light-front holographic radiative transition form factors for light mesons. *Phys. Rev. D*, 102:034021, Aug 2020.
- [5] Mohammad Ahmady, Spencer Keller, Michael Thibodeau, and Ruben Sandapen. Reexamination of the rare decay $B_s \rightarrow \phi\mu^+\mu^-$ using holographic light-front qcd. *Phys. Rev. D*, 100:113005, Dec 2019.
- [6] Mohammad Ahmady, Chandan Mondal, and Ruben Sandapen. Dynamical spin effects in the holographic light-front wavefunctions of light pseudoscalar mesons. *Phys. Rev. D*, 98:034010, Aug 2018.
- [7] T. M. Aliev and M. Savcı. Exclusive $\vec{B} \rightarrow \pi l^+ l^-$ and $\vec{B} \rightarrow \rho l^+ l^-$ decays in the two higgs doublet model. *Phys. Rev. D*, 60:014005, May 1999.
- [8] Patricia Ball, Vladimir M Braun, and Alexander Lenz. Twist-4 distribution amplitudes of the k^* and mesons in qcd. *Journal of High Energy Physics*, 2007(08):090–090, Aug 2007.
- [9] Patricia Ball and Roman Zwicky. New results on $B \rightarrow K$ decay form factors from light-cone sum rules. *Physical Review D*, 71(1), jan 2005.
- [10] Stanley J. Brodsky. Qcd phenomenology and light-front wavefunctions. 2001. hep-ph/0111340.
- [11] Stanley J. Brodsky and Guy F. de Téramond. AdS/CFT and Light-Front QCD, 2008. arXiv:0802.0514.
- [12] Stanley J. Brodsky and Guy F. de Téramond. *Search for the “Totally Unexpected” in the LHC Era*, pages 139–183.

- [13] Stanley J. Brodsky, Guy F. de T eramond, Hans G unter Dosch, and Joshua Erlich. Light-front holographic qcd and emerging confinement. *Physics Reports*, 584:1–105, Jul 2015.
- [14] Sophia S. Chabysheva and John R. Hiller. Dynamical model for longitudinal wave functions in light-front holographic qcd. *Annals of Physics*, 337:143–152, 2013.
- [15] Guy F. de T eramond and Stanley J. Brodsky. Longitudinal dynamics and chiral symmetry breaking in holographic light-front qcd. *Physical Review D*, 104(11), Dec 2021.
- [16] P.A. Zyla et. al. (Particle Data Group), Prog. Theor. Exp. Phys. 2020. 083C01 (2020) and 2021 update.
- [17] David J Griffiths. *Introduction to elementary particles; 2nd rev. version*. Physics textbook. Wiley, New York, NY, 2008.
- [18] Ronald R. Horgan, Zhaofeng Liu, Stefan Meinel, and Matthew Wingate. Lattice qcd calculation of form factors describing the rare decays $B \rightarrow K^* \ell^+ \ell^-$ and $B_s \rightarrow \phi \ell^+ \ell^-$. *Physical Review D*, 89(9), May 2014.
- [19] G. 't Hooft. A two-dimensional model for mesons. *Nuclear Physics B*, 75(3):461–470, 1974.
- [20] Wikipedia. Standard model, 2021.
- [21] Liping Zou and H. G. Dosch. A very practical guide to light front holographic qcd, 2018. arXiv:1801.00607.

Appendix A

Sample Code for Calculating Meson Masses

Below is a sample piece of Wolfram Mathematica code illustrating how the 't Hooft equation was solved. The predicted pion mass (highlighted) is in GeV.

```
(*Normalization constant for basis function*)
norm1[n_, beta1_, beta2_] :=
  Sqrt[(2 n + 2 beta1 + 2 beta2 + 1)  $\frac{n! \text{Gamma}[n + 2 \text{beta1} + 2 \text{beta2} + 1]}{\text{Gamma}[n + 2 \text{beta1} + 1] \text{Gamma}[n + 2 \text{beta2} + 1]}$ ]

(*Basis function*)
fthooft[x_, n_, beta1_, beta2_] :=
  norm1[n, beta1, beta2] xbeta1 (1 - x)beta2 JacobiP[n, 2 beta2, 2 beta1, 2 x - 1]

(*Matrices for diagonalization*)
A1thooft[beta1_, beta2_] :=
  NIntegrate[ $\frac{\text{fthooft}[x, n, \text{beta1}, \text{beta2}] \times \text{fthooft}[x, m, \text{beta1}, \text{beta2}]}{x}$ , {x, 0, 1}] // Quiet

A2thooft[beta1_, beta2_] :=
  NIntegrate[ $\frac{\text{fthooft}[x, n, \text{beta1}, \text{beta2}] \times \text{fthooft}[x, m, \text{beta1}, \text{beta2}]}{1 - x}$ , {x, 0, 1}] // Quiet

Bthooft[beta1_, beta2_] :=
 $\frac{1}{2}$  NIntegrate[ $\frac{\text{fthooft}[x, n, \text{beta1}, \text{beta2}] - \text{fthooft}[y, n, \text{beta1}, \text{beta2}]}{x - y}$ , {y, 0, 1}, {x, 0, 1}] // Quiet
 $\frac{\text{fthooft}[x, m, \text{beta1}, \text{beta2}] - \text{fthooft}[y, m, \text{beta1}, \text{beta2}]}{x - y}$ , {y, 0, 1}, {x, 0, 1}] // Quiet

(*Eigensystem used to solve for expansions coefficients*)
matrizeqn[m1_, m2_, g_, beta1_, beta2_, r_] :=
  Table[m12 A1thooft[beta1, beta2] + m22 A2thooft[beta1, beta2] +  $\frac{g^2}{\text{pi}}$  Bthooft[beta1, beta2],
    {n, 0, r}, {m, 0, r}]

(*Meson mass using equations (6) and (19) from Ahmady et. al. 2021*)
mass[m1_, m2_, beta1_, beta2_, g_, kappa_, r_, i_, L_, nT_] :=
  Sqrt[Eigenvalues[matrizeqn[m1, m2, g, beta1, beta2, r]][[i]] + 4 kappa2 (nT + L)]

(*Test case for pion*)
Highlighted[mass[0.046, 0.046, 0.34, 0.34, 0.128, 0.523, 5, -1, 0, 0]]

Out[ ] = 0.140422
```